

# Reconstruction of Past Antarctic Temperature Using Present Seasonal $\delta^{18}\text{O}$ –Inversion Layer Temperature: Unified Slope Equations and Applications

Z. LIU<sup>1</sup>, C. HE,<sup>a,b,c</sup> M. YAN,<sup>d,b</sup> C. BUIZERT,<sup>e</sup> B. L. OTTO-BLIESNER,<sup>f</sup> F. LU,<sup>g</sup> AND C. ZENG<sup>d,b</sup>

<sup>a</sup> Department of Geography, The Ohio State University, Columbus, Ohio

<sup>b</sup> Laoshan Laboratory, Qingdao, China

<sup>c</sup> College of Atmospheric Sciences, Nanjing University of Information Science and Technology, Nanjing, China

<sup>d</sup> College of Geography Science, Nanjing Normal University, Nanjing, China

<sup>e</sup> College of Earth, Ocean, and Atmospheric Sciences, Oregon State University, Corvallis, Oregon

<sup>f</sup> Climate and Global Dynamics Laboratory, National Center for Atmospheric Research, Boulder, Colorado

<sup>g</sup> Geophysical Fluid Dynamic Laboratory, NOAA, Princeton, New Jersey

(Manuscript received 10 January 2022, in final form 7 November 2022, accepted 20 December 2022)

**ABSTRACT:** Reconstructing the history of polar temperature from ice core water isotope ( $\delta^{18}\text{O}$ ) calibration has remained a challenge in paleoclimate research, because of our incomplete understanding of various temperature– $\delta^{18}\text{O}$  relationships. This paper resolves this classical problem in a new framework called the unified slope equations (USE), which illustrates the general relations among spatial and temporal  $\delta^{18}\text{O}$ –surface temperature slopes. The USE is applied to the Antarctica temperature change during the last deglaciation in model simulations and observations. It is shown that the comparable Antarctica-mean spatial slope with deglacial temporal slope in  $\delta^{18}\text{O}$ –surface temperature reconstruction is caused, accidentally, by the compensation responses between the  $\delta^{18}\text{O}$ –inversion layer temperature relation and the inversion layer temperature itself. Furthermore, in light of the USE, we propose that the present seasonal slope of  $\delta^{18}\text{O}$ –inversion layer temperature is an optimal paleothermometer that is more accurate and robust than the spatial slope. This optimal slope suggests the possibility of reconstructing past Antarctic temperature changes using present and future instrumental observations.

**SIGNIFICANCE STATEMENT:** This paper develops a new framework called the unified slope equations (USE) to provide, for the first time, a general relation among various spatial and temporal water isotope–temperature slopes. The application of the USE to Antarctic deglacial temperature change shows that the optimal paleothermometer is the seasonal slope of the inversion layer temperature.


**KEYWORDS:** Atmosphere; Inversions; Climate records; Isotopic analysis

## 1. Introduction

The stable water isotope ratio  $^{18}\text{O}/^{16}\text{O}$  ( $\delta^{18}\text{O}$ ) in ice cores is critical for our understanding of global climate change because it provides a key proxy for reconstructing past polar surface temperature  $T_s$  (e.g., Jouzel et al. 2003). However, a quantitative interpretation of  $\delta^{18}\text{O}$  requires the use of the correct isotope sensitivity, or  $\delta^{18}\text{O}$ – $T$  slope,  $\alpha = d\delta^{18}\text{O}/dT$  (in  $\text{‰ K}^{-1}$ ). Yet  $\alpha$  has been found widely different among various spatial and temporal slopes, and at different locations. For example, in Antarctica, spatial  $\delta^{18}\text{O}$ – $T_s$  regression gives a spatial slope on surface temperature  $\alpha_{s,T_s} \approx 0.8\text{‰ K}^{-1}$  on average in observations and climate models (Jouzel et al. 2003; Masson-Delmotte et al. 2008; Sime et al. 2008, 2009; Werner et al. 2018), with substantial regional variations from  $0.5\text{‰}$  to

$1.2\text{‰ K}^{-1}$  (Masson-Delmotte et al. 2008; Werner et al. 2018). Over Greenland, the spatial slope  $\alpha_{s,T_s}$  has been found to underestimate the  $T_s$  changes by  $\sim 50\%$  relative to independent estimations (Cuffey et al. 1995; Severinghaus et al. 1998), caused mainly by the change of precipitation seasonality during deglaciation (Krinner et al. 1997; Werner et al. 2000). Over Antarctica, nevertheless, the change of precipitation seasonality for long-term climate changes is small. As such, the Antarctica-mean  $\alpha_{s,T_s}$  ( $\approx 0.8\text{‰ K}^{-1}$ ) appears roughly comparable with the deglacial slope  $\alpha_{\text{deg},T_s}$ , which is often estimated using the difference between Last Glacial Maximum (LGM) and the preindustrial (PI), in climate models and independent temperature estimations in observations, such as borehole and  $\Delta$ age-based temperatures (e.g., Buizert et al. 2021). This has led to the tendency to use the Antarctica-mean  $\alpha_{s,T_s}$  as an empirical surrogate for  $\alpha_{\text{deg},T_s}$  (Jouzel et al. 2003; Masson-Delmotte et al. 2008; Cuffey et al. 2016; Werner et al. 2018).

In spite of much effort to understand the relation between spatial and deglacial temporal slopes (Boyle 1997; Sime et al. 2008, 2009; Noone 2009; Guan et al. 2016), much confusion remains. Various mechanisms have been proposed that may distort the deglacial slope away from that of the Rayleigh process, including the changes of source temperatures and ice volume (Boyle 1997) as well as moisture origins (Charles et al. 1994). An empirical effort has been made to find a present

 Denotes content that is immediately available upon publication as open access.

He's current affiliation: Rosenstiel School of Marine and Atmospheric Science, University of Miami, Miami, Florida.

Corresponding authors: Z. Liu, liu.7022@osu.edu; C. He, cxh1079@rsmas.miami.edu

DOI: 10.1175/JCLI-D-22-0012.1

© 2023 American Meteorological Society. For information regarding reuse of this content and general copyright information, consult the AMS Copyright Policy ([www.ametsoc.org/PUBSReuseLicenses](http://www.ametsoc.org/PUBSReuseLicenses)).

Brought to you by University of Colorado Libraries | Unauthenticated | Downloaded 04/21/23 07:47 PM UTC

temporal slope for paleotemperature reconstruction using the seasonal  $\delta^{18}\text{O}-T_s$  slope  $\alpha_{\text{sea},T_s}$ . However,  $\alpha_{\text{sea},T_s}$  is found to range from 0.27‰ to 0.58‰  $\text{K}^{-1}$  in observations, less than half of the Antarctica-mean spatial slope  $\alpha_{s,T_s}$  (van Ommen and Morgan 1997; Motoyama et al. 2005; Schneider et al. 2005). Finally, it has long been recognized that it is important to study the temperature response of not only surface temperature  $T_s$  but also condensation temperature  $T_c$ , along with the  $\delta^{18}\text{O}-T_c$  slope, because  $T_c$  is the temperature that determines the precipitation  $\delta^{18}\text{O}$  in Rayleigh theory (Dansgaard 1964; Jouzel and Merlivat 1984). This  $T_c$ , which can often be approximated by the inversion layer temperature, differs significantly from the surface temperature  $T_s$  over the Antarctic, because of the strong inversion layer there, especially in winter (Jouzel and Merlivat 1984). These studies seem to suggest the relevance of, at least, three pairs of  $\delta^{18}\text{O}-T_s$  and  $\delta^{18}\text{O}-T_c$  slopes to the reconstruction of Antarctic temperature: two deglaciation slopes  $\alpha_{\text{deg},T_s}$  and  $\alpha_{\text{deg},T_c}$ , two spatial slopes  $\alpha_{s,T_s}$  and  $\alpha_{s,T_c}$ , and two seasonal slopes of  $\alpha_{\text{sea},T_s}$  and  $\alpha_{\text{sea},T_c}$ . So far, however, there has been no general understanding of the relationships among these slopes from a unified perspective, and, furthermore, which one is the optimal for reconstructing paleotemperatures. Our study is motivated to address these issues. Specifically, this paper will address two fundamental questions on the  $\delta^{18}\text{O}-T$  slope:

- Question 1a: Mechanistically, why does the spatial slope  $\alpha_{s,T_s}$  as a whole appear to be comparable with the deglacial slope  $\alpha_{\text{deg},T_s}$  over Antarctica?

This question involves a more general question:

- Question 1b: What is the relation among these different aforementioned isotope slopes in general?
- Question 2: Practically, what slope is the most suitable for estimating past temperature changes over Antarctica?

Here, we study spatial and temporal slopes in general by developing a set of unified slope equations (USE) that illustrate the general relation between spatial and temporal slopes. As an application, we apply USE to the reconstruction of past Antarctic temperature change over the last deglaciation. First, we test USE in an isotope-enabled Earth system model (iCESM; Brady et al. 2019), in which the paleotemperature is known. Our study suggests that it is an accident that the spatial slope  $\alpha_{s,T_s}$  appears comparable with the deglacial slope  $\alpha_{\text{deg},T_s}$ . Furthermore, unexpectedly, the optimal paleothermometer that reconstructs surface temperature  $T_s$  more robustly and accurately than the spatial slope is the present seasonal slope on inversion layer temperature  $T_c$ , or  $\alpha_{\text{sea},T_c}$ . Then, we apply this optimal paleothermometer to the reconstruction of deglacial temperature in observations, and the results seem to be in reasonable agreement with independent reconstructions.

Our paper is organized in three parts. The first part (section 2) introduces major concepts and describes the major features of isotope slopes, their relationships, as well as the response of the inversion layer temperatures, in our model iCESM. The second part (section 3) is the core of the paper. Here, we

develop a general relationship between spatial and temporal slopes called USE and then use the USE framework to understand the relationships among spatial, deglacial, and seasonal slopes. The third part (section 4) develops the optimal paleothermometer as  $\alpha_{\text{sea},T_c}$  and applies it to the reconstruction of deglacial temperatures over Antarctica in light of the USE framework. This optimal paleothermometer is first validated in iCESM in section 4a and is then applied to observations in section 4b. Major conclusions are given in section 5.

## 2. Spatial and temporal slopes in iCESM

### a. The iCESM

We first briefly describe the state-of-the-art Earth system model iCESM, which is the model for our discussions and methodology validation. Our model employed is the Community Earth System Model version 1.3 with fully coupled water isotope modules. Of interest here, the atmosphere model has a nominal  $2^\circ$  resolution in both latitude and longitude. In the vertical, the model atmosphere has 30 levels with a hybrid sigma-pressure coordinate such that the vertical coordinate follows surface topography near the surface (for details, see the CESM document at <https://www.cesm.ucar.edu/models/atm-cam/docs/usersguide/node25.html>). The hybrid level is represented as a weighted pressure in the unit of pressure  $\tilde{P}$  (hPa). Over Antarctica, the hybrid levels of  $\tilde{P} = 980$  and 800 hPa correspond approximately to about 100 and 1000 m above the surface, respectively. Stable water isotopes are incorporated into all iCESM components: the atmosphere, ocean, land surface, river runoff, and sea ice, and iCESM simulates the water isotopes consistent with the model hydroclimate of the present day, as discussed extensively in previous studies (Nusbaumer et al. 2017; Brady et al. 2019). Here, we will analyze a transient iCESM simulation of the last deglacial period (from 21 000 to 11 000 years ago) (iTRACE), which is forced by realistic radiative forcing, atmospheric greenhouse gases, continental ice sheets, and melting water fluxes [see He et al. (2021a,b) for details]. This simulation has also been shown to reproduce the deglacial evolution of precipitation  $\delta^{18}\text{O}$  and  $T_s$  over Greenland in good agreement with paleo-observations (He et al. 2021b). The simulated  $\delta^{18}\text{O}-T_s$  slopes are also largely consistent with recent independent reconstructions over the Antarctic, as discussed in Buizert et al. (2021) and more extensively later in our paper.

### b. Spatial and deglacial slopes on surface temperatures $T_s$

The overall deglacial slope and spatial slope of  $\delta^{18}\text{O}-T_s$  over Antarctica are comparable in iCESM (Fig. 1). Figure 1a shows the scatter diagram of annual mean  $T_s$  against annual precipitation weighted  $\delta^{18}\text{O}$  over each model gridcell point over Antarctica for two snapshots at the LGM (20 ka BP) and PI (1850) (He et al. 2021a,b). It is seen that in both PI (black plus) and LGM (gray plus), the overall spatial slope is about  $\alpha_{s,T_s} \sim 0.9\% \text{K}^{-1}$ , similar to other models of about  $0.8\% - 1.0\% \text{K}^{-1}$  (Jouzel et al. 2003; Lee et al. 2008; Masson-Delmotte et al. 2008; Werner et al. 2018). A visual inspection shows that this spatial slope appears comparable with the deglacial slope  $\alpha_{\text{deg},T_s}$ , or  $\alpha_{s,T_s} \sim \alpha_{\text{deg},T_s}$ . Here,  $\alpha_{\text{deg},T_s}$  are represented as straight (blue) lines that connect

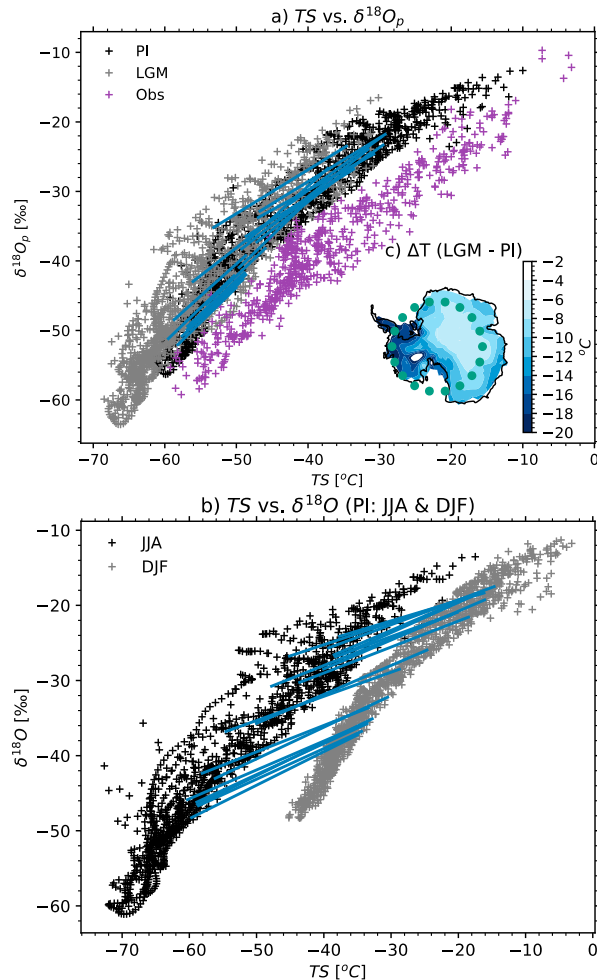


FIG. 1.  $\delta^{18}\text{O}$  and surface temperature in the Antarctic. (a) Mean annual  $\delta^{18}\text{O}_p$  (precipitation weighted) vs surface air temperature  $T_s$  at preindustrial (PI; black) and Last Glacial Maximum (LGM; gray) in iCESM and in the present observation (purple) (Masson-Delmotte et al. 2008); (b) as in (a), but for  $\delta^{18}\text{O}_p$  in the season of DJF and JJA at PI. In (a) [(b)], the 18 blue lines connect the PI and LGM (DJF and JJA) to represent the deglacial temporal (seasonal) slopes in 18 box regions (each of  $20^\circ \times 20^\circ$ ) centered at the green dots shown in (c) the inset. This figure gives an overall impression that the deglacial slope is comparable with the spatial slope, while the seasonal slope is about half that of the spatial slope for surface temperature.

pairs of LGM and PI values of the same region for 18 ( $20^\circ \times 20^\circ$ ) box regions around the Antarctica (shown in the inset Fig. 1c). This spatial slope for annual mean is also similar to those calculated for different seasons. For example, Fig. 1b shows the similar scatterplot but for winter (JJA, black plus) and summer (DJF, gray plus) seasonal values at PI. It is seen that the  $\delta^{18}\text{O}$  and  $T_s$  for winter and summer both show an overall spatial slope comparable with the annual spatial slope in Fig. 1a. It is also interesting to note here that the spatial slope is larger than the seasonal slope  $\alpha_{\text{sea}, T_s}$  by a factor of about 2, the latter being represented as straight (blue) lines connecting the two seasons

over 18 regions around the Antarctica circle in Fig. 1b. The seasonal slope will be discussed in more detail later.

Regionally, spatial slopes  $\alpha_{s, T_s}$  vary substantially around the Antarctica-mean value of  $0.9\text{‰ K}^{-1}$ , as shown in the scatter diagram in Fig. 2d (the  $x$  axis). These  $\alpha_{s, T_s}$  values increase with decreasing  $T_s$ , from coastal regions of about  $0.5\text{‰ K}^{-1}$  to interior East Antarctica Plateau of about  $1.5\text{‰ K}^{-1}$  as shown in the spatial map in Fig. 2a. Note, however, spatial slope changes with the domain size, a point to be returned later. Here, in Figs. 2a and 2d, spatial slope is calculated as the regression of about 25 gridcell points in each  $10^\circ \times 10^\circ$  box. This domain size is a compromise for our model between the need of sufficient grid points and the ability to resolve regional features of the slope.

The model deglacial slope  $\alpha_{\text{deg}, T_s}$  is calculated as the difference between the LGM and PI states after removing the globally uniform  $+0.1\text{‰ K}^{-1}$  enrichment effect due to the moisture accumulation in the continental ice sheet. (Similar deglacial slopes can also be calculated as the regression from the iTRACE time series from LGM to 11 ka.) These model  $\alpha_{\text{deg}, T_s}$  values have been shown largely consistent with the latest independent estimation using borehole thermometry and firn properties for seven ice cores: Dome C (DC), Dome Fuji (DF), EPICA Dronning Maud Land (EDML), South Pole (SP), Talos Dome (TAL), West Antarctica Ice Sheet (WD), and Siple Dome (SDM) (Buizert et al. 2021), which are also shown in the spatial map in Fig. 2b (their values are in the filling color of the same scale as the model). The deglacial slope in iCESM is  $\alpha_{\text{deg}, T_s} \sim 1\text{‰ K}^{-1}$  averaged over Antarctica, which is slightly higher than the spatial slope  $\alpha_{s, T_s}$  for the Antarctica mean, as shown in the scatter diagram between  $\alpha_{\text{deg}, T_s}$  and  $\alpha_{s, T_s}$  in Fig. 2d, leading to a deglacial slope roughly comparable with the Antarctica-mean spatial slope, i.e.,

$$\alpha_{s, T_s} \approx \alpha_{\text{deg}, T_s}, \quad (2.1)$$

consistent with the visual impression in Fig. 1a. Regionally, however, a spatial slope can differ substantially from the deglacial slope, as seen in the regional scatter across the Antarctica in Fig. 2d, a point to be returned later. Here, (2.1) raises the question why, mechanistically, the spatial slope averaged over the Antarctica appears to be comparable with the deglacial slope. As shown below, this comparable slope is an “accident” of compensation between different inversion layer temperature responses and different  $\delta^{18}\text{O}$ –inversion temperature slopes. Therefore, to understand (2.1), we need to examine the responses of the inversion layer temperature as well as the relation between spatial and temporal slopes in general, which will be discussed next in sections 2c and 3, respectively.

### c. Spatial and deglacial slopes on inversion layer temperature $T_c$

Over the Antarctica, condensation temperature can be approximated by the inversion layer temperature, or the warmest tropospheric temperature at the top of the surface-based inversion layer (Masson-Delmotte et al. 2008). In iCESM, the vertical temperature profiles in the PI and LGM simulations (for both winter and summer in Figs. 3a,b) show that the

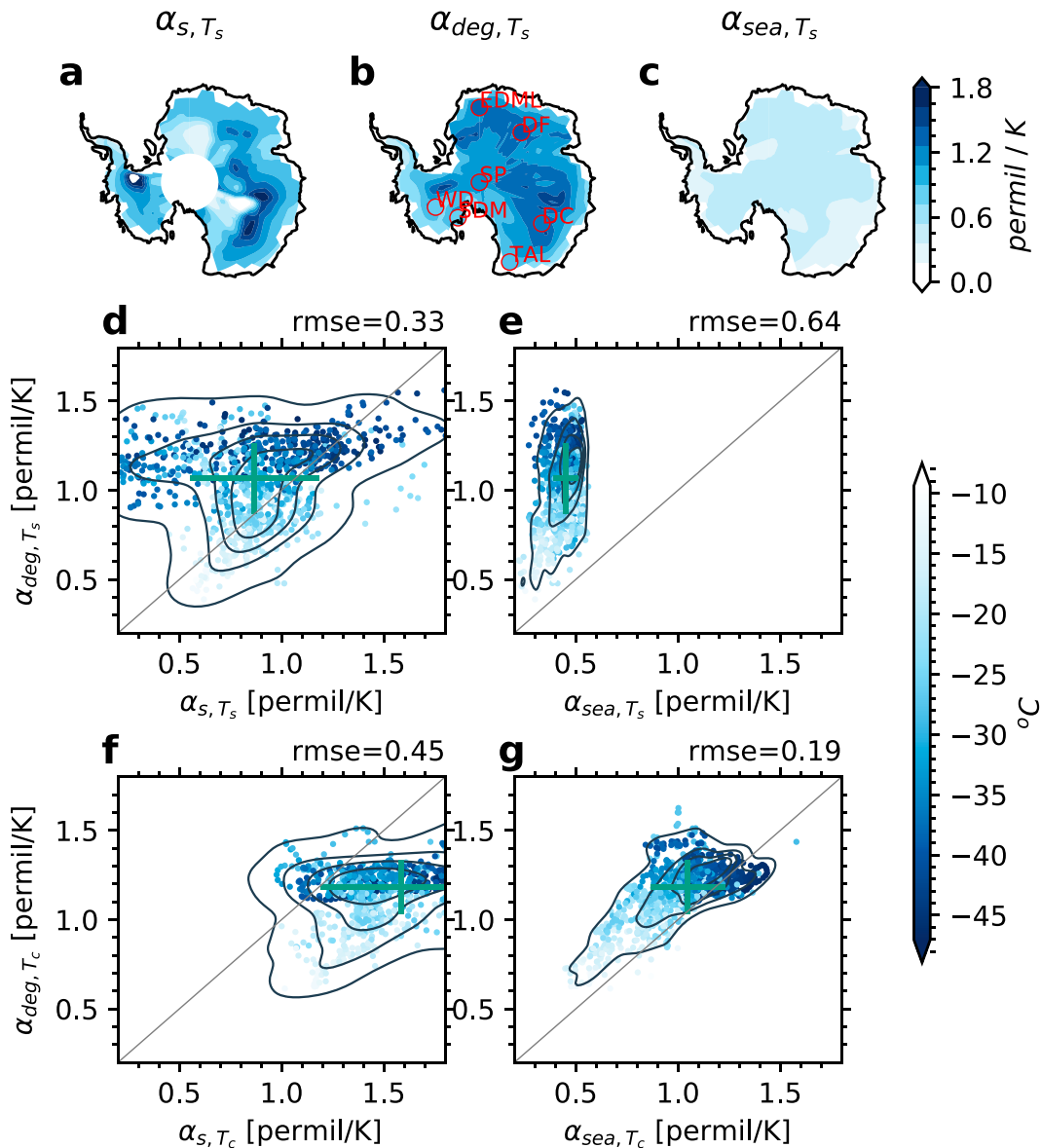


FIG. 2. Deglacial temporal slopes, spatial slopes, and seasonal temporal slopes and their relationship over the Antarctica in iCESM. (a) Spatial slope calculated from surface air temperature  $\alpha_{s, T_s}$ ; (b) As in (a), but for deglacial temporal slope  $\alpha_{deg, T_s}$ ; (c) as in (a), but for seasonal temporal slope  $\alpha_{sea, T_s}$ ; (d) scatter diagram of spatial slope vs deglacial slope for surface air temperatures across Antarctic grid points; (e) as in (d), but for the scatter of seasonal slope vs deglacial slope; (f), (g) as in (d) and (e), but for slopes calculated from the inversion layer temperature  $T_c$  (calculated as the average between hybrid sigma-pressure levels 980 and 800 hPa, about 100 and 1000 m above the surface)  $\alpha_{s, T_c}$ ,  $\alpha_{deg, T_c}$  and  $\alpha_{sea, T_c}$ . In (d)–(g), the shadings of the dots are the corresponding surface temperatures; black contours are the PDFs of each cluster. The green cross is the mean of the cluster with one standard deviation in each direction as the wings. In (a), (d), and (f), the spatial slope at each gridcell point is calculated as the regression coefficient between  $\delta^{18}\text{O}$  and temperature within a  $10^\circ \times 10^\circ$  box centered at the grid. To avoid large sampling errors, spatial slopes south of  $85^\circ\text{S}$  are not calculated. The RMSEs in (d)–(g) are the root-mean-square difference between the slope values on the  $x$  and  $y$  axis over all gridcell points on Antarctica, and a smaller RMSE means that the two slopes are similar (closer to the diagonal line). All spatial and seasonal slopes in this figure are averaged between LGM and PI. (All major features remain the same if LGM or PI is used alone.) In (b), the circles represent the ice core  $\alpha_{deg, T_s}$  from the recent independent reconstructions on seven ice cores (Buizert et al. 2021), with the value as the color scale inside the circle, which has the same scale as that in the model (shading).

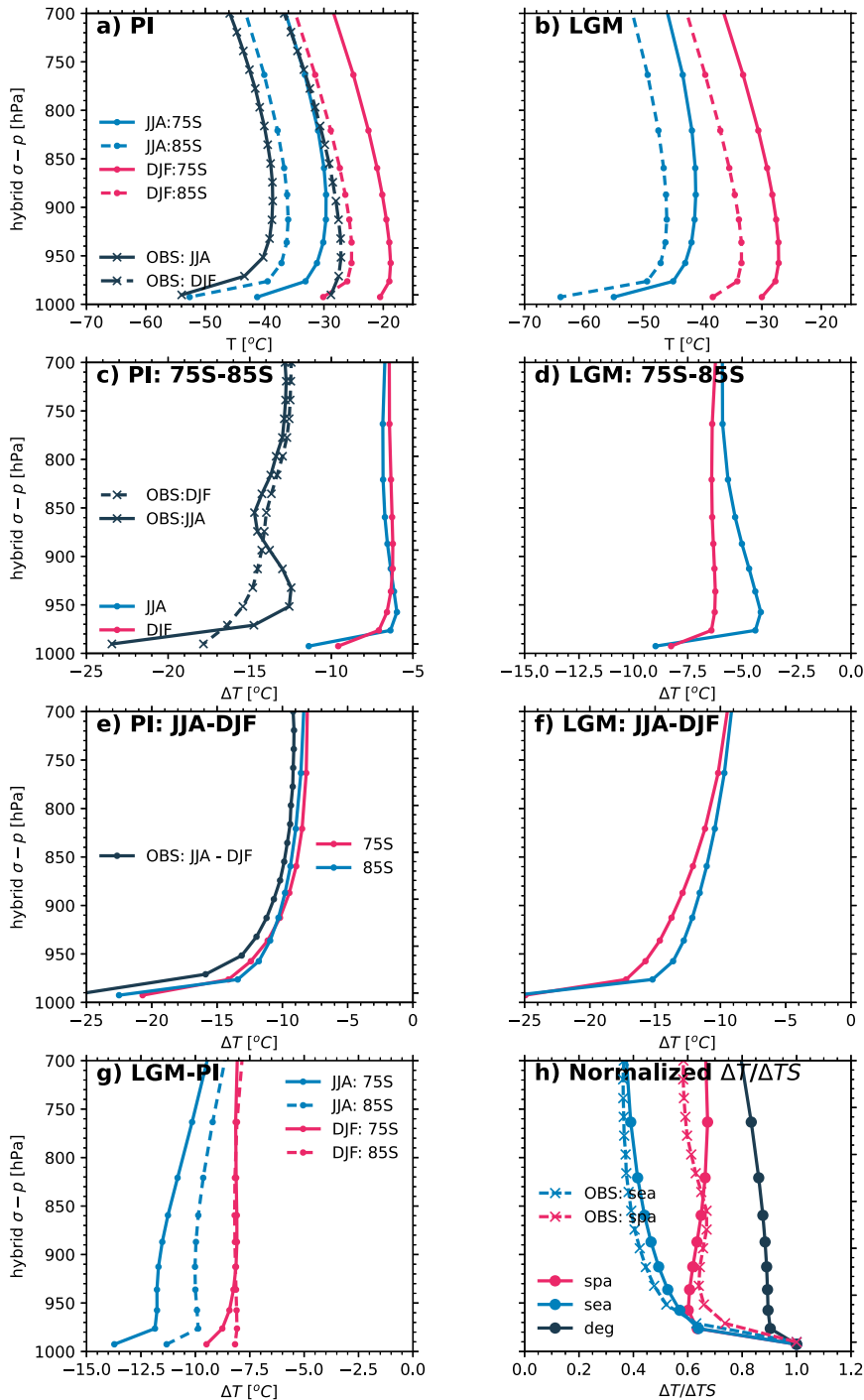


FIG. 3. Temperature vertical profiles and their changes in Antarctica. (a) Temperature profiles regionally averaged over  $70^{\circ}$ – $80^{\circ}$ S and  $80^{\circ}$ – $90^{\circ}$ S (nominally denoted as  $75^{\circ}$  and  $85^{\circ}$ S, respectively) in Antarctica for summer (DJF) and winter (JJA) in PI. (b) As in (a), but in LGM. (c) Spatial difference between regional means of  $80^{\circ}$ – $90^{\circ}$ S and  $70^{\circ}$ – $80^{\circ}$ S (denoted as  $75^{\circ}$ – $85^{\circ}$ S) for summer (DJF) and winter (JJA) in PI. (d) As in (c), but in LGM. (e) Seasonal difference (denoted as JJA – DJF) of regional temperatures at PI. (f) As in (e), but for LGM. (g) Deglacial change from LGM to PI (denoted as LGM – PI) of regional temperatures of JJA and DJF. (h) Spatial [average of (c) and (d)], seasonal [average of (e) and (f)] and deglacial [average of (g)] changes normalized by their corresponding surface temperature changes  $\Delta T_s$ . The observations averaged for stations Byrd, Vostok, and South Pole, are also shown in (a), (c), (e), and (h), except for the spatial difference, which is calculated as the difference between Byrd and the mean of Vostok and South Pole. The vertical coordinates are the native hybrid sigma-pressure level for model and, similarly,  $1000p/p_s$  ( $p$  and  $p_s$  are the pressures of the observation level and the surface) for observation.



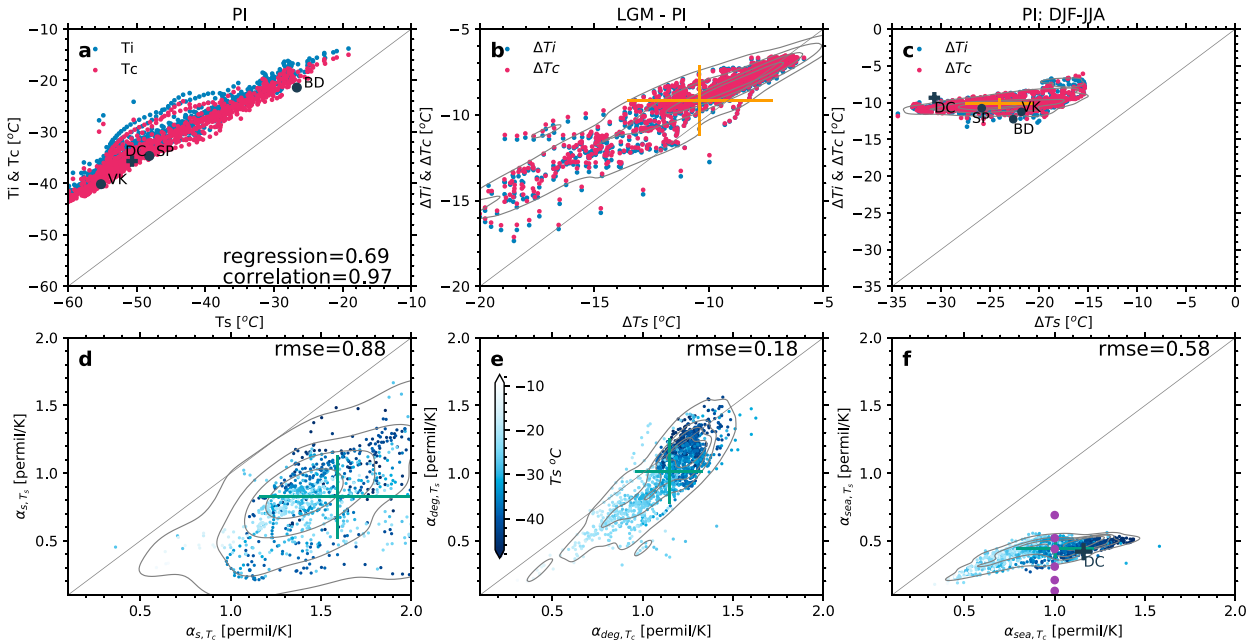


FIG. 4. Relationship between slopes and temperatures at surface and inversion layer. (a) Surface air temperature  $T_s$  vs mean inversion (maximum) temperature  $T_i$  in red ( $T_c$  in red). (b) As in (a), but for temperature difference between LGM and PI (LGM – PI). (c) As in (b), but for temperature difference between JJA and DJF at PI (JJA – DJF). Note the different representations between the spatial change in (a) on the temporal change in (b) and (c). The spatial change is represented by the spread of points in (a), but a temporal change is represented by a single point (instead of the spread) in (b) or (c). (d) Spatial slopes for inversion ( $\alpha_{s,T_c}$ ) vs surface ( $\alpha_{s,T_s}$ ) temperatures. (e) As in (d), but for deglacial slopes  $\alpha_{deg,T_c}$  vs  $\alpha_{deg,T_s}$ . (f) As in (e), but for seasonal slopes  $\alpha_{sea,T_c}$  vs  $\alpha_{sea,T_s}$ . Spatial and seasonal temporal slopes here are averaged between LGM and PI. In (b)–(f), the gray contours are the PDFs of each cluster with the crosses as the ensemble mean and standard deviations. In (a) and (c), the four black markers are derived from updated station observations, consistent with previous studies (Jouzel and Merlivat 1984; Connolley 1996). In (f),  $\alpha_{sea,T_s}$  values are plotted for six stations (purple dots) in observations (van Ommen and Morgan 1997; Schneider et al. 2005; Motoyama et al. 2005), plotted on  $\alpha_{sea,T_c} = 1$  and Dome C (Stenni et al. 2016) (black plus). The colors in (d)–(f) are the annual mean surface temperature of PI climatology with the color bar in the inset of (e). In (d)–(f), the RMSE are the root-mean-square difference between the slope values on the  $x$  and  $y$  axis over all gridcell points in Antarctica.

inversion layer temperature, as indicated by the warmest temperature above surface, occurs usually about 300 m above the ground (about the 950-hPa hybrid level). Therefore,  $T_c$  can be approximated well by the temperature averaged between about 100 and about 1000 m above ground (precisely between the model hybrid sigma-pressure levels 980 and 800 hPa). This similarity between the inversion layer temperature and the mean temperature from 100 to 1000 m above ground can also be seen for PI (Fig. 4a) and LGM-PI (Fig. 4b) across the Antarctica in the scatter diagram, as the two temperatures (blue and red dots) almost overlap.

A comparison of the spatial and deglacial slopes on inversion temperature against the corresponding slopes on surface temperature across the Antarctica show that the deglacial slopes remains largely unchanged between inversion and surface temperatures  $\alpha_{deg,T_c} \approx \alpha_{deg,T_s}$  (along the diagonal one-to-one line in Fig. 4e), but the spatial slope on surface temperature  $\alpha_{s,T_s}$  is smaller than that on inversion temperature  $\alpha_{s,T_c}$  by  $\sim 50\%$  (below the diagonal one-to-one line in Fig. 4d), that is,

$$\alpha_{deg,T_c} \approx \alpha_{deg,T_s}, \quad (2.2a)$$

but

$$\alpha_{s,T_c} > \alpha_{s,T_s}. \quad (2.2b)$$

Since the Antarctica-mean  $\alpha_{s,T_s}$  is comparable with  $\alpha_{deg,T_s}$  as in (2.1), the relations of (2.2a) and (2.2b) also imply a greater spatial slope than deglacial slope on inversion temperature:

$$\alpha_{s,T_c} > \alpha_{deg,T_c}. \quad (2.3)$$

This is indeed seen across the Antarctica more clearly in direct comparison of these two slopes, with the scatter over each grid point predominantly below the diagonal one-to-one line (Fig. 2f).

The different  $T_c$  slopes in (2.3) and the comparable  $T_s$  slopes in (2.1) between spatial and deglacial changes are caused by the different inversion layer responses between spatial and deglacial changes. Across space, the change of inversion temperature  $\Delta T_c$  and surface temperature  $\Delta T_s$  in the model is represented by the spread of  $T_c$  and  $T_s$  in Fig. 4a. (In the paper, “ $\Delta$ ” represents a difference either in space or time.) The regression slope is 0.69 (Fig. 4a), indicating that the spatial change of  $\Delta T_c$  is smaller than that of  $\Delta T_s$  with  $\Delta T_c/\Delta T_s \sim 0.69$ . This is also consistent with weather station observations in previous works (Jouzel and Merlivat 1984;

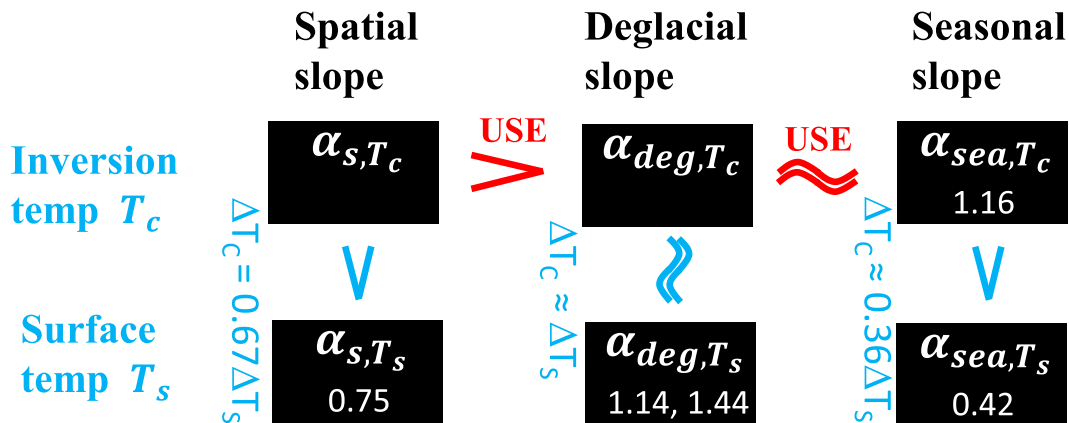


FIG. 5. Relations among slopes in light of USE and inversion layer responses. The numbers are for Dome C observations. The two numbers of  $\alpha_{deg, T_s}$  are the two independent temperature reconstructions from borehole thermometry and gas age–ice age difference (Buizert et al. 2021).

Masson-Delmotte et al. 2008) and in our analysis of updated observations (black marks in Fig. 4a) (appendix A). In contrast, during deglaciation, the inversion temperature change is almost comparable with the surface temperature with  $\Delta T_c/\Delta T_s \sim 0.9$  (Fig. 4b), as indicated by the PDF center of  $\Delta T_c$  versus  $\Delta T_s$ . [Note the different representation between Figs. 4a and 4b: the deglacial change at a model grid cell is plotted as a point (instead of the spread) in Fig. 4b, while the spatial change across model grid cell is represented by the spread in Fig. 4a. Therefore, the PDF center in Fig. 4b represents the mean value of the deglacial changes of  $\Delta T_c/\Delta T_s$ , while the spread in Fig. 4b only represents the regional difference of deglacial change over Antarctica.] The different inversion layer responses between spatial and deglacial changes are seen more intuitively in the vertical profiles of regional Antarctic temperatures and their changes (Figs. 3a,b). The spatial change can be represented as the difference between the latitude bands of 85°S (80°–90°S average) and 75°S (70°–80°S average) for the same season (DJF or JJA) and the same time period (PI or LGM) (Figs. 3c,d), while the deglacial change can be represented as the difference between LGM and PI for the same latitude band (75°S or 85°S) and the same season (DJF or JJA) (Fig. 3g). A comparison of the spatial change and deglacial change shows a much stronger cooling in  $T_s$  (bottom layer) than in  $T_c$  (layers above) across space (Figs. 3c,d) than deglaciation (Fig. 3g), especially in winter. This stronger surface cooling with space at PI is also consistent with current station observations for both seasons (Fig. 3c, connected crosses). A more quantitative comparison between the spatial and deglacial changes can be made by comparing the vertical profiles of the change normalized by their respective difference at the surface: this normalized temperature profile shows that the inversion layer change relative to surface is  $\Delta T_c/\Delta T_s \sim 0.67$  for spatial change, but  $\Delta T_c/\Delta T_s \sim 0.9$  for deglaciation (red connected dot versus black connected dot in Fig. 3h), consistent with the scatterplot across the Antarctica discussed in Figs. 4a and 4b. Furthermore, this feature of a smaller spatial change than deglacial change in  $\Delta T_c/\Delta T_s$  is robust across models (appendix B,

Fig. B1). Thus, the seemingly comparable spatial and deglacial slopes on  $T_s$  for Antarctica in Eq. (2.1) is an “accident” that is caused by a smaller spatial change of inversion temperature  $\Delta T_c/\Delta T_s$  multiplied by a larger spatial  $T_c$  slope  $\alpha_{s, T_c}$ . These relations among different spatial and deglacial slopes are summarized in Fig. 5 (left and middle columns).

This “accident” of  $\alpha_{s, T_s} \approx \alpha_{deg, T_s}$  raises two questions:

Q1: Why is the  $T_c$  response larger for deglaciation change than for spatial change, or

$$\Delta T_c/\Delta T_s|_{deg} \approx 1 > \Delta T_c/\Delta T_s|_{spatial} \quad (2.4)$$

Q2: Why is the spatial  $T_c$  slope greater than the deglacial  $T_c$  slope as in (2.3),

$$\alpha_{s, T_c} > \alpha_{deg, T_c}?$$

The first question involves the response of vertical temperature profiles to different climate forcing. The larger deglacial  $\Delta T_c/\Delta T_s$  change is forced by the GHG forcing, which tends to force a vertically uniform temperature response, while the smaller  $\Delta T_c/\Delta T_s$  change across space is caused by the solar radiation forcing, which tends to force a stronger temperature change in the surface than above (see appendix B for a more detailed discussion). The second question is a central question of this work and will be addressed in detail in section 3.

It is interesting to note that the response of inversion layer temperature profile across space is similar to that in seasonal changes, albeit one in space and the other in time. This occurs because both are forced by solar radiation forcing (appendix B). In iCESM,  $\Delta T_c/\Delta T_s < 0.5$  as shown in the scatter diagram Fig. 4c and the vertical profiles (DJF–JJA, Figs. 3e,f,h, B1, B2). This small seasonal change of  $\Delta T_c/\Delta T_s$  is robust in different models (appendix B, Fig. B1) and the present weather station observations (Fig. 4c, black marks; Connolley 1996).

Combining all the discussions above on the inversion layer responses, we have that the  $T_c$  response (relative to  $T_s$  response,

i.e.,  $\Delta T_c/\Delta T_s$ ) is greater for deglaciation change than for both the spatial and seasonal responses, i.e.,

$$\Delta T_c/\Delta T_s|_{\text{deg}} \approx 1 > \Delta T_c/\Delta T_s|_{\text{spatial}} \sim \Delta T_c/\Delta T_s|_{\text{seasonal}}. \quad (2.5)$$

These inversion layer responses are summarized in Fig. 5. Important for applications later, the different inversion layer responses suggest that the deglacial response of  $\Delta T_c$  should be approximated by the surface change as  $\Delta T_c \approx \Delta T_s$ , instead of the traditionally assumed  $\Delta T_c = 0.67\Delta T_s$  derived for spatial changes.

### 3. The framework of unified slope equations

Now, we study one central question of the paper: Why is the spatial  $T_c$  slope greater than the deglacial  $T_c$  slope  $\alpha_{s,T_c} > \alpha_{\text{deg},T_c}$  as in (2.3)? We first derive a general relation between spatial and temporal slopes based on the Rayleigh processes in response to global-scale climate changes, called the USE (sections 3a and 3b), and then use the USE framework to understand the relations between spatial and temporal slopes (section 3c) and among spatial, deglacial, and seasonal slopes (section 3d).

#### a. Rayleigh distillation process and Lagrangian slope $\alpha_L$

In the Rayleigh distillation process (Dansgaard 1964), in a bulk of air mass, an infinitesimal change of condensation  $\delta^{18}\text{O}$  with temperature is determined by (Jouzel and Merlivat 1984)

$$\alpha_L = \frac{d\delta}{dT} = (1 + \delta) \left\{ \frac{(a-1)}{q} \frac{dq}{dT} + \frac{1}{a} \frac{da}{dT} \right\} \approx \frac{(a-1)}{q} \frac{dq}{dT} + \frac{1}{a} \frac{da}{dT}, \quad (3.1)$$

where  $q$  is the moisture content and  $a(T)$  is the equilibrium fractionation coefficient that decreases slightly with temperature. In iCESM,  $a(T)$  adopts three equations: the first for liquid to vapor in warm temperatures ( $T > 273.15$  K), the second for liquid to ice in cold temperatures ( $T < 253.15$  K), and the third as a linear combination of the first two for temperatures in between ( $273.15 \text{ K} > T > 253.15 \text{ K}$ ) (Nusbaumer et al. 2017) (Fig. 6a).

Throughout section 3, for simplicity and without confusion,  $\delta^{18}\text{O}$  will be denoted as  $\delta$ , and  $T$  should be understood as the condensation temperature or inversion temperature  $T_c$ , instead of the surface temperature  $T_s$ , unless otherwise specified, because we only deal with the idealized Rayleigh process. The contribution from the specific humidity  $q$  to  $\alpha_L$  in (3.1) can be further decomposed to three terms associated with saturation vapor pressure  $e^*$ , supersaturation  $S^*$ , and pressure  $p$ ,

$$c_q = \frac{1}{q} \frac{dq}{dT} = \frac{1}{e^*} \frac{de^*}{dT} + \frac{1}{S^*} \frac{dS^*}{dT} - \frac{1}{p} \frac{dp}{dT} = c_C + c_S + c_P. \quad (3.2a)$$

With the three processes denoted as

$$c_C = \frac{1}{e^*} \frac{de^*}{dT}, \quad c_S = \frac{1}{S^*} \frac{dS^*}{dT}, \quad c_P = -\frac{1}{p} \frac{dp}{dT}. \quad (3.2b)$$

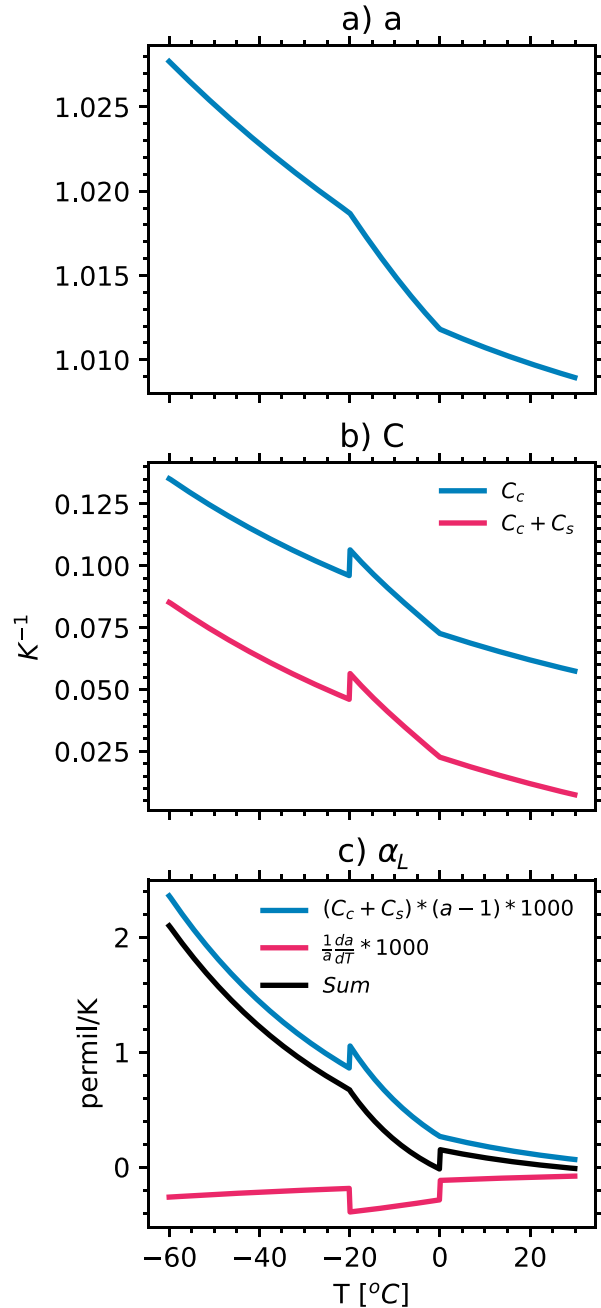


FIG. 6. Rayleigh model and parameters as functions of temperature for (a) the fractionation coefficient, (b) relative changes of saturation vapor pressure  $c_C$  and total vapor  $c_q$  as defined in Eq. (3.2b) and the supersaturation rate  $c_S = -0.05$ , and (c) Lagrangian slope  $\alpha_L$  and its components as defined in Eq. (3.1) in the modified Rayleigh model.

Here, we have used  $q = 0.62e_v/p = 0.62S^*e^*(T)/p$ , with  $e_v$  being the vapor pressure,  $e^*(T)$  being the saturation vapor pressure over water/ice at the water/ice temperature, and  $S^* = e_v/e^*(T)$ .

The slope  $\alpha_L(T)$  depends only on the temperature of the air mass, regardless of its Lagrangian trajectory in space or



time and its source, and therefore will be called the Lagrangian slope. The  $\alpha_L$  increases toward colder temperature, roughly from  $\sim 0.6\text{‰ K}^{-1}$  at  $-10^\circ\text{C}$  to  $\sim 1.2\text{‰ K}^{-1}$  at  $-50^\circ\text{C}$ , mainly due to the Clausius–Clapeyron rate (Fig. 6c). This change of  $\alpha_L$  is dominated by the Clausius–Clapeyron rate  $c_C$ . For decreasing temperature from  $-10^\circ$  to  $-50^\circ\text{C}$ ,  $c_C$  increases from  $\sim 0.085$  to  $\sim 0.12 \text{ K}^{-1}$  (Fig. 6b). Since the fractionation coefficient  $a - 1$  also increases from  $\sim 0.015$  to  $\sim 0.024 \text{ K}^{-1}$  (Fig. 6a), the corresponding Lagrangian slope  $(a - 1)c_C$  increases from  $\sim 1.2\text{‰}$  to  $\sim 2.8\text{‰ K}^{-1}$ . This slope is reduced by 15% by the pressure effect of  $c_P \sim -0.015 \text{ K}^{-1}$  (Jouzel and Merlivat 1984). This  $c_P$  reduction can be estimated by rewriting  $c_P = (1/H)\partial z/\partial T = -1/(HT)$ , where  $\Gamma = -\partial T/\partial z \sim 10^\circ\text{C km}^{-1}$  is the lapse rate and the pressure is assumed varying with a scale height of  $H \sim 7 \text{ km}$  as  $p = p_0 e^{-z/H}$ . The kinetic fractionation effect associated with supersaturation has been assumed of around  $c_S \sim -0.05 \text{ K}^{-1}$  (Ciais and Jouzel 1994; Markle and Steig 2022). This  $c_S$  reduces the  $c_C$  contribution to  $\alpha_L$  by  $\sim 40\%$ . The  $c_S$  value, nevertheless, has a large uncertainty and can also be considered to include the effects of mixing processes (Eriksson 1965; Hendricks et al. 2000; Kavanaugh and Cuffey 2003; Noone 2008; Siler et al. 2021). Finally, the  $\alpha_L$  is reduced by another  $\sim 15\%$  by the fractionation coefficient change as  $(1/a)da/dT \sim -0.25\text{‰ K}^{-1}$  (Fig. 6c) as in (3.1), leading to a final  $\alpha_L$  that increases from  $0.6\text{‰}$  to  $1.2\text{‰ K}^{-1}$ , comparable with the analysis of iCESM output. This increasing  $\alpha_L$  with colder temperature will be reflected in all spatial and temporal slopes, as will be discussed later.

Given a Lagrangian slope  $\alpha_L(T)$ , the isotope ratio  $\delta$  can be calculated by the integration of the fractionation from the source temperature  $T_0$  in what we call the Lagrangian isotope function:

$$\delta = L(T, T_0) = \int_{T_0}^T \alpha_L(\tilde{T}) d\tilde{T}. \quad (3.3)$$

As an example, in a modified Rayleigh model,  $\delta$  value is obtained by integrating (3.1) analytically using the central-value theorem approximation (Dansgaard 1964) as

$$\delta \approx \frac{a(T)}{a(T_0)} \left[ \frac{q(T)}{q(T_0)} \right]^{a_m^{-1}} - 1, \quad (3.4)$$

where  $a_m = [a(T) + a(T_0)]/2$  and  $q = 0.62S^*e^*(T)/p$ . Here,  $T$  and  $p$  are in situ temperature and pressure, which can be derived from the iCESM model output, while  $T_0$  and  $p_0$  are the temperature and pressure of each source region, as can be obtained from the additional tagging experiment (appendix C). We note, however, that the absolute value of  $\alpha_L$  is not critical to our major conclusions, because our focus is on the relative magnitudes between temporal and spatial slopes.

Now, we assume that there are multiple moisture sources over the world, each of a fixed geographic region, a source temperature  $T_{0i}$  and a moisture weight  $w_i = O_i^{16}/O^{16}$  ( $i = 1, 2, \dots, n$ ). As an example, these source regions can be seen in our tagging experiments in Figs. B2a and B2b. The contribution on the condensation  $\delta^{18}\text{O}$  from each source is then determined from (3.3) as

$$\delta_i = L(T, T_{0i}) = \int_{T_{0i}}^T \alpha_L(\tilde{T}) d\tilde{T}. \quad (3.5)$$

The total  $\delta$  can be shown as a weighted sum, plus the global ice volume effect  $\delta_d(t)$ , as

$$\delta = \sum_{i=1}^N \delta_i w_i + \delta_d(t), \quad (3.6)$$

where the total weight sums up to 1

$$\sum_{i=1}^n w_i = 1. \quad (3.7)$$

If we apply the modified Rayleigh model (3.4) to iCESM climate, we find this Rayleigh model approximates the iCESM water isotope in the Antarctica reasonably well (Fig. 7), which is another evidence that the Rayleigh process is the dominant process for Antarctic water isotope in iCESM, consistent with other studies (Bailey et al. 2019; Markle and Steig 2022).

#### b. USE

We can derive two general equations that link spatial and temporal slopes via the Lagrangian slope, in the USE. First, given the independence of  $\alpha_L$  with source region in (3.5), the Lagrangian slope can be derived as

$$\frac{\partial \delta_i}{\partial T} = \frac{\partial L(T, T_{0,i})}{\partial T} = \alpha_L(T), \quad (3.8)$$

and therefore from (3.6) and (3.7),

$$\frac{\partial \delta}{\partial T} = \sum_{i=1}^n \alpha_L(T) w_i = \alpha_L(T). \quad (3.9)$$

#### 1) SPATIAL SLOPE $\alpha_s$ IN USE

The site temperature varies in space  $x$  and time  $t$  as  $T(x, t)$ . Here,  $t$  is the time for which the temporal slope is evaluated. For example,  $t$  is the calendar month if one calculates the temporal slope of the seasonal cycle. For deglacial slope,  $t$  is the time (annual mean, each calendar month or season) during the deglaciation after a low pass filtering of, say, 10- or 100-yr average, to remove the influence of shorter variability. The source temperature (of a fixed geographic region “ $i$ ”) varies only with time  $T_{0i}(t)$ . Thus, the climatic  $\delta^{18}\text{O}$  contribution from source  $i$  in (3.5) can be written as

$$\delta_i(x, t) = L[T(x, t), T_{0i}(t)]. \quad (3.10)$$

Furthermore, the moisture weight also varies spatially and temporally as  $w_i(x, t)$ . Thus, the total isotope ratio in (3.6) can be rewritten as a function of space and time as

$$\delta(x, t) = \sum_{i=1}^n \delta_i(x, t) w_i(x, t) + \delta_d(t). \quad (3.11)$$

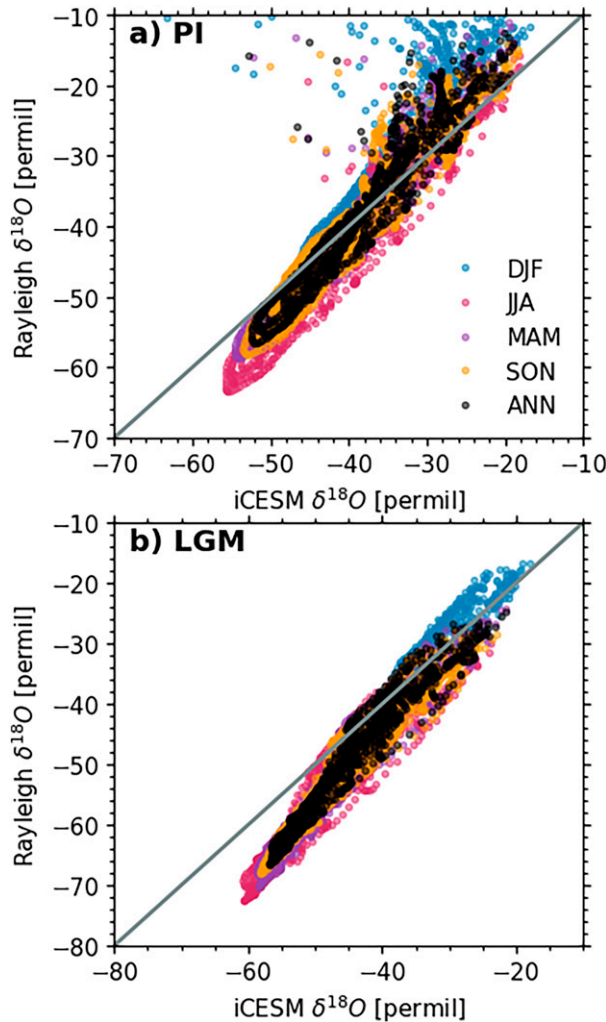


FIG. 7.  $\delta^{18}\text{O}$  reconstructed from Rayleigh model in Antarctica. (a)  $\delta^{18}\text{O}$  reconstructed from the Rayleigh model compared to iCESM at PI across Antarctica for four seasons and the annual mean. (b) As in (a), but for LGM. The  $\delta^{18}\text{O}$  is reconstructed using the “bottom-up” scheme.

For infinitesimal changes, the spatial slope can be derived as

$$\begin{aligned}\alpha_s(x, t) &= \left. \frac{\partial}{\partial T} \delta(x, t) \right|_{l=\text{const}} = \frac{\partial \delta(x, t)}{\partial x} \bigg/ \frac{\partial T(x, t)}{\partial x} \\ &= \frac{1}{\frac{\partial T}{\partial x}} \sum_{i=1}^n \left\{ \frac{\partial \delta_i}{\partial x} w_i + \delta_i \frac{\partial w_i}{\partial x} \right\} \\ &= \frac{1}{\frac{\partial T}{\partial x}} \sum_{i=1}^n \left\{ \frac{\partial L(T, T_{0i})}{\partial T} \frac{\partial T}{\partial x} w_i + \delta_i \frac{\partial w_i}{\partial x} \right\}.\end{aligned}$$

With (3.8)–(3.11), we therefore have the USE spatial slope equation

$$\alpha_s(x, t) = \alpha_L(T) + \sum_{i=1}^n \delta_i \frac{\partial w_i}{\partial T}. \quad (3.12)$$

This shows that spatial slope is contributed by  $\alpha_L$  and the spatial variation of weights.

## 2) TEMPORAL SLOPE $\alpha_t$ IN USE

The temporal slope  $\alpha_t$  can be derived similarly as

$$\begin{aligned}\alpha_t(x, t) &= \left. \frac{\partial}{\partial T} \delta(x, t) \right|_{x=\text{const}} = \frac{\partial \delta(x, t)}{\partial t} \bigg/ \frac{\partial T(x, t)}{\partial t} \\ &= \frac{1}{\frac{\partial T}{\partial t}} \left\{ \sum_{i=1}^n \left( \frac{\partial \delta_i}{\partial t} w_i + \delta_i \frac{\partial w_i}{\partial t} \right) + \frac{d\delta_d}{dt} \right\} \\ &= \frac{1}{\frac{\partial T}{\partial t}} \left\{ \sum_{i=1}^n \left[ \left( \frac{\partial L}{\partial T} \frac{\partial T}{\partial t} + \frac{\partial L}{\partial T_{0i}} \frac{\partial T_{0i}}{\partial t} \right) w_i + \delta_i \frac{\partial w_i}{\partial t} \right] + \frac{d\delta_d}{dt} \right\}.\end{aligned}$$

Note that the change of source temperature with time introduces an additional source term  $\sim \partial T_{0i}/\partial t$  that is not present in the spatial slope equation. Since from (3.5), we have in general

$$\frac{\partial L(T, T_{0i})}{\partial T_{0i}} = -\alpha_L(T_{0i}). \quad (3.13)$$

The USE temporal slope equation can be written as

$$\alpha_t(x, t) = \alpha_L(T) - \sum_{i=1}^n \alpha_L(T_{0i}) w_i \frac{\partial T_{0i}}{\partial T} + \sum_{i=1}^n \delta_i \frac{\partial w_i}{\partial T} + \frac{d\delta_d}{dt}. \quad (3.14)$$

The  $\alpha_t$  is contributed by  $\alpha_L$ , the weight change with time (third term), and additionally, the change of source temperature (second term), in addition to the global ice volume (the fourth term). Individually, the mechanism associated with each term has been recognized in previous work: the  $\delta$ – $T$  relation and, in turn, the deglacial slope is due fundamentally to the Rayleigh process via  $\alpha_L(T)$  (Dansgaard 1964), modified by source temperature and ice volume (Boyle 1997), and the moisture origin (Charles et al. 1994), which is equivalent to the change of weight here. Here, USE, for the first time, provides two general relations for temporal, spatial, and Lagrangian slopes that incorporate these mechanisms together, quantitatively. USE is general because it only requires  $\alpha_L$  being a function of  $T$  as in (3.1) or (3.8), and therefore, the Lagrangian function (3.5) or (3.10) is valid, regardless of the functional details of  $\alpha_L(T)$ . Thus, USE provides us a general framework to assess the relative importance of each mechanism, quantitatively.

### c. Relations between spatial and temporal slopes in USE framework

The USE provides a quantitative relation between temporal and spatial slopes. The spatial and temporal equations of USE in (3.12) and (3.14) show that both the spatial and temporal slopes depend critically on, but generally do not equal to, the Lagrangian slope, because of the changes in weight,

source temperature, and global ice volume. In the simplest case of a single source, the USEs (3.12) and (3.14) are reduced to

$$\alpha_s(x, t) = \alpha_L(T), \tag{3.15}$$

$$\alpha_t(x, t) = \alpha_L(T) \left[ 1 - \frac{\alpha_L(T_0)}{\alpha_L(T)} \frac{\partial T_0}{\partial T} \right] + \frac{d\delta_d}{\partial T}. \tag{3.16}$$

Therefore, both  $\alpha_s$  and  $\alpha_t$  are proportional to  $\alpha_L$  and, therefore, are of comparable magnitudes of  $\alpha_L$  on the order of  $\sim 1\text{‰ K}^{-1}$  (Fig. 6c). Their magnitudes tend to increase with decreasing temperature (color of dots in Fig. 2f) as does  $\alpha_L$  following the Rayleigh process, contributed mainly by the saturation vapor pressure change (Figs. 6b,c). This change of slope with temperature is important because it implies that the paleothermometer changes with time, instead of being time invariant. Indeed, the smaller deglacial slope at higher temperature has been proposed to lead to a greater warming than that from the traditional reconstruction using the time-invariant slope, implying a higher interglacial warming in the past than thought previously (Sime et al. 2009; Noone 2009).

Combining Eqs. (3.15) and (3.16) gives a relation between the spatial and temporal slopes as

$$\alpha_t(x, t) = \alpha_s(x, t) \left[ 1 - r \frac{\partial T_0}{\partial T} \right] + \frac{d\delta_d}{\partial T}, \tag{3.17}$$

with the source temperature sensitivity  $r$  as

$$r = \frac{\alpha_L(T_0)}{\alpha_L(T)}. \tag{3.18}$$

This equation is reminiscent of the semiempirical slope equation of Guan et al. (2016) where, nevertheless, the sensitivity  $r$  is prescribed a priori. Here, we can show in general  $\alpha_L(T_0) < \alpha_L(T)$  and therefore  $0 < r < 1$ . This follows because the moisture source to polar region originates usually from lower latitudes where the climatological temperature is warmer than the polar region,  $T_0 > T$ , and the Lagrangian slope  $\alpha_L(T)$  in general increases with decreasing temperature (Fig. 6c). Thus, Eqs. (3.17) and (3.18) suggest that the temporal slope for glacial cycles is always smaller than the spatial slope (neglecting the small contribution from the ice volume change of  $\sim 0.1\text{‰ K}^{-1}$ ), or

$$\alpha_t(x, t) < \alpha_s(x, t), \tag{3.19}$$

as long as temperature changes are the same sign in the source region and polar region, i.e.,

$$\frac{\partial T_0}{\partial T} / \frac{\partial T}{\partial t} > 0,$$

except in the unrealistic case of a strong ‘‘tropical amplification’’ to global climate change such that  $\partial T_0/\partial t$  is much larger than  $\partial T/\partial t$ . It is also important to recognized that the same sign of  $\partial T_0/\partial t$  and  $\partial T/\partial t$  is usually satisfied for global-scale climate change, which often exhibit a polar amplification (Guan et al.

2016). The importance of the source temperature change in reducing the temporal slope from spatial slope is consistent with the qualitative schematic scheme by Boyle (1997). Note, however, since the temperatures here is the condensation temperature  $T_c$ , the application to surface temperature  $T_s$  can be changed by the inversion layer response, in particularly in the Antarctica, where the inversion layer is strong (Jouzel and Merlivat 1984), a point to be returned later.

The reduced temporal slope from spatial slope in the single source case can be generalized, approximately, to the general case for multiple sources. Indeed, in both USEs, the total contribution from the weight changes is usually small relative to the Lagrangian slope term, as will be confirmed later in our iCESM analysis (see appendix D and discussions on Fig. D1). This occurs because the total weight always sums to 1 as in (3.7), and therefore  $\sum_{i=1}^n \partial w_i = 0$ . Thus, the change of weights  $\partial w_i$  has to have opposite signs among all sources, leading to cancelations of  $\delta_i \partial w_i$  among different source regions (note  $\delta_i$  are always the same sign). In other words, the increases of weights in some regions will be compensated by the decreases of the weights from some other regions, which are nevertheless all of comparable  $\delta$  values. This point is seen clearly in the simple case of two regions, when the weight term reduces to  $\sum_{i=1}^2 \delta_i \partial w_i = (\delta_1 - \delta_2) \partial w_1$  as a second-order residual term. Therefore, at the leading order, the spatial slope Eq. (3.12) can be approximated as

$$\alpha_s(x, t) \approx \alpha_L(T). \tag{3.20}$$

With (3.20), the temporal slope (3.14) can also be approximated as

$$\alpha_t(x, t) \approx \alpha_s(x, t) \left( 1 - \sum_{i=1}^n r_i \frac{\partial T_{0i}}{\partial T} \right), \tag{3.21}$$

where

$$r_i = \frac{\alpha_L(T_{0i}) w_i}{\alpha_L(T)}, \tag{3.22}$$

and we have neglected the small contribution from the ice volume change. It should be noted that, unlike the total weight change term that is usually negligible, the source temperature term cannot be neglected. This follows because the weight  $w_i$  is always positive, and, for global-scale climate changes, the source temperature change  $\partial T_{0i}$  tends to be of the same sign across different source regions. Therefore, the contributions from different source temperatures are accumulated, as opposed to be canceled as in the weight term. Since

$$\sum_{i=1}^n r_i \frac{\partial T_{0i}}{\partial T} < \sum_{i=1}^n \frac{\alpha_L(T_{0m}) w_i}{\alpha_L(T)} \frac{\partial T_{0m}}{\partial T} = \frac{\alpha_L(T_{0m})}{\alpha_L(T)} \frac{\partial T_{0m}}{\partial T} < 1,$$

where  $\alpha_L(T_{0m})(\partial T_{0m}/\partial t) = \max_{i=1,n} [\alpha_L(T_{0i})(\partial T_{0i}/\partial t)]$  is the largest source temperature change, we have the similar conclusion as in the single source case in (3.19) as  $\alpha_t(x, t) < \alpha_s(x, t)$  in general.

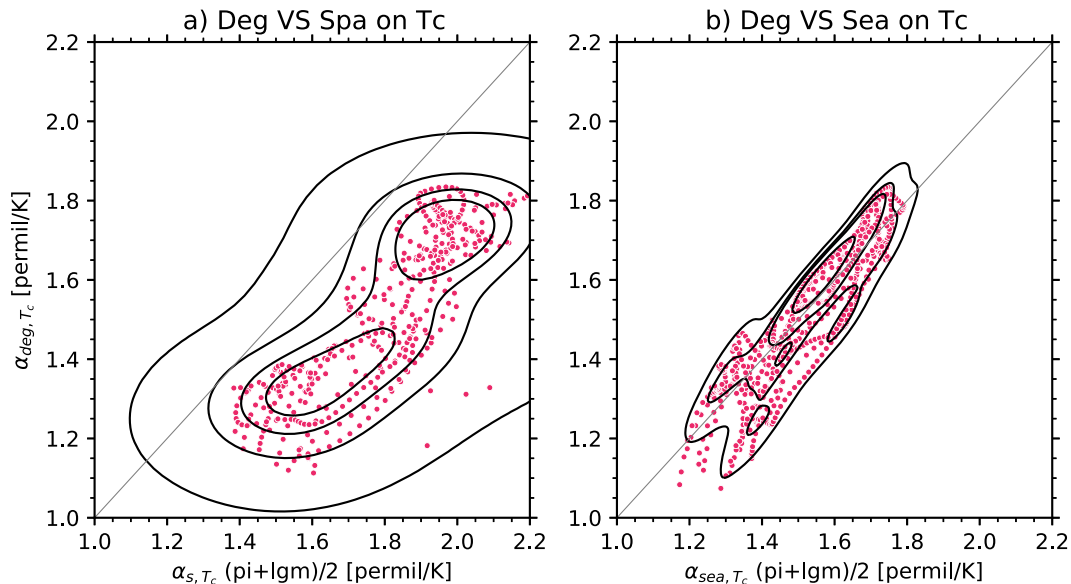


FIG. 8. Relationship among slopes in the Antarctica in the Rayleigh model. (a) Spatial slope ( $\alpha_{s,T_c}$ ) vs deglacial slope ( $\alpha_{\text{deg},T_c}$ ) calculated on the iCESM inversion temperature  $T_c$ . (b) As in (a), but for seasonal temporal slope ( $\alpha_{\text{sea},T_c}$ ) vs deglacial slope. The spatial and seasonal slopes are the average of LGM and PI. Note, for  $\alpha_{s,T_c}$  ( $\alpha_{\text{sea},T_c}$ ), we use the average between LGM and PI, because  $\alpha_{s,T_c}$  ( $\alpha_{\text{sea},T_c}$ ) differs slightly between LGM and PI and the average is used as the mean representation.

We caution that the uncertainty of the ignorance of weight changes needs to be reevaluated when realistic synoptic variability is considered. As pointed out by one reviewer, several *in situ* and satellite observation studies (e.g., Turner et al. 2019) suggested that the precipitation weighting effect induced by synoptic-scale perturbation cannot be neglected over Antarctica. They were statistically supported by the latest isotope–GCM study (Kino et al. 2021). This perspective may have impact on the weight change term (third term) in Eq. (3.14) and later in the relation among different slopes in Eq. (4.2). It is therefore important to study the weight change using improved climate model with better representation of synoptic processes in the future.

#### d. Spatial slope, deglacial slope, and seasonal slope

A direct application of USE inequality (3.19) to deglacial evolution in iTRACE is a smaller deglacial slope than spatial slope on the inversion temperature as in (2.3):  $\alpha_{\text{deg},T_c} < \alpha_{s,T_c}$ . This inequality has been seen in the iCESM in Fig. 2f, and is also confirmed in our modified Rayleigh model across Antarctica (Fig. 8a). Quantitatively, the reduction effect associated with source temperature in (3.21) is about  $\sim 30\%$  of  $\alpha_L$  during the deglaciation as estimated using the USE decomposition analysis (appendix D) of the deglacial change (the second row in Figs. D1a,b). Furthermore, this reduction amount is not very sensitive to the details of the sources as discussed in appendix E in Fig. E1.

An interesting and important deduction from USE is that the deglacial slope on  $T_c$  should equal approximately to the seasonal  $T_c$  slope, i.e.,

$$\alpha_{\text{deg},T_c} \approx \alpha_{\text{sea},T_c}. \quad (3.23)$$

This follows because the temporal slope Eq. (3.14) applies to any temporal slope, including the seasonal and deglacial slopes. Furthermore, seasonal temperature change is also of hemispheric scale (Fig. B2b) such that Antarctic temperature change should be of the same sign as those over its major moisture sources, which are all located in the Southern Hemisphere (Markle et al. 2017; Bailey et al. 2019), similar to deglaciation (Figs. E1a4,a5 versus Figs. E1b4,b5, see discussions in appendix E). Thus,  $\alpha_{\text{sea},T_c}$  should also be reduced from  $\alpha_L$  similar to  $\alpha_{\text{deg},T_c}$ . This is confirmed in the USE decompositions in iCESM and our modified Rayleigh model (Figs. D1a,b, third rows similar to second rows in Figs. D1a,b). Combining (2.3) and (3.23) leads to the relation among the three  $T_c$  slopes as

$$\alpha_{\text{deg},T_c} \approx \alpha_{\text{sea},T_c} < \alpha_{s,T_c}. \quad (3.24)$$

This is confirmed in iCESM and our Rayleigh model, where the scatter of  $\alpha_{\text{sea},T_c}$  against  $\alpha_{\text{deg},T_c}$  are largely along the diagonal one-to-one line in iCESM (Fig. 2g) and Rayleigh model (Fig. 8b), in contrast to the scatter of  $\alpha_{s,T_c}$  against  $\alpha_{\text{deg},T_c}$ , which stays systematically below the diagonal line in iCESM (Fig. 2f) and Rayleigh model (Fig. 8a).

The temporal slope equation also offers one explanation why the temporal slope for large-scale global climate change, such as deglaciation and seasonal cycle, differ dramatically from that of present day internal variability of interannual to interdecadal time scales, as noticed in previous studies (e.g., Sime et al. 2008). Internal climate variability is forced predominantly by regional SST changes, such as in ENSO, PDO, and AMV. These temperature changes are of regional scale,

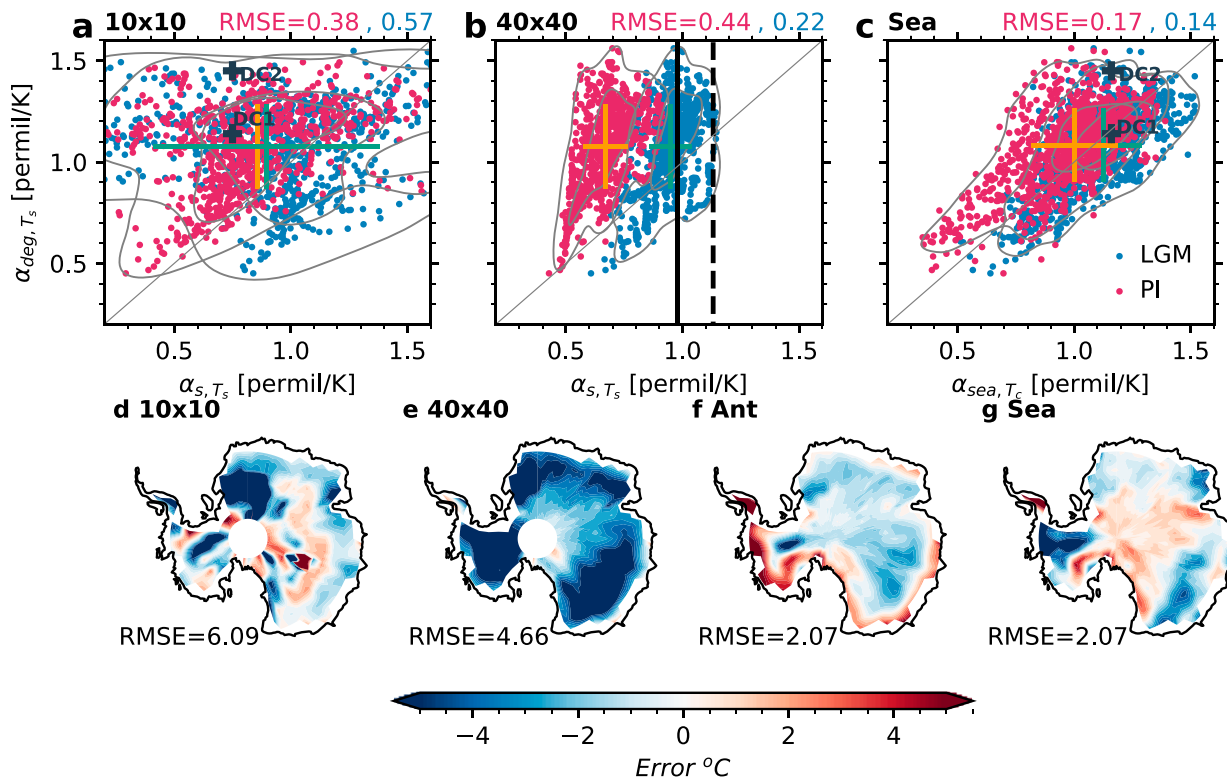


FIG. 9. Paleothermometers of seasonal vs spatial slopes and predicted  $T_s$  in iCESM. (a)  $\alpha_{s,T_s}$  (PI, red dots; LGM, blue dots) regressed in the  $10^\circ \times 10^\circ$  domain vs  $\alpha_{deg,T_s}$  for all grid points over Antarctica. (b) As in (a), but for  $\alpha_{s,T_s}$  in  $40^\circ \times 40^\circ$  domain. (c) As in (a) and (b), but for  $\alpha_{sea,T_c}$  vs  $\alpha_{deg,T_s}$  on each model grid point; (d) error of reconstructed LGM-PI  $T_s$  change by the  $\alpha_{s,T_s}$  of  $10^\circ \times 10^\circ$  domain. (e)–(g) As in (d), but by the  $\alpha_{s,T_s}$  of  $40^\circ \times 40^\circ$  domain, Antarctic domain, and seasonal slope  $\alpha_{sea,T_c}$  on each gridcell point, respectively. In (a)–(c), gray contours are the PDFs of each cluster, with the green and yellow bars as the ensemble mean and standard deviations of the LGM (blue) and PI (red) slopes, along with their RMSE ( $\% \text{ K}^{-1}$ ) at the top. In (b), vertical black lines are for the  $\alpha_{s,T_s}$  regressed over the Antarctic domain at PI [solid, used in (f)] and LGM (dash). In (e)–(g), the RMSE ( $^\circ\text{C}$ ) of predicted  $T_s$  are at the bottom left. Dome C observations are marked in two  $\alpha_{deg,T_s}$  reconstructions (in black pluses) for temperature reconstructions based on borehole and gas age–ice age difference (Buizert et al. 2021) against the  $\alpha_{s,T_s}$  (Lorius and Merlivat 1975) and  $\alpha_{sea,T_c}$  (Stenni et al. 2016) in (a) and (c), respectively.

instead of basin scale. As such,  $\partial T_0/\partial t$  are far from homogeneous, and may therefore differ significantly from the polar temperature change  $\partial T/\partial t$ , even with opposite signs.

We note that, for convenience of the application of USE, all deglacial sensitivities  $\alpha$  in this paper are calculated using the  $\delta^{18}\text{O}$  of the same season or arithmetic annual mean without precipitation weight. Real-world ice core isotopes are precipitation weighted. Over Antarctica, however, this sensitivity is virtually the same as with and without precipitation weight, because of the small change of precipitation seasonality, as also discussed in previous studies (Jouzel et al. 2003; Werner et al. 2018). So the USE application to Antarctica is straightforward.

#### 4. Applications

##### a. Optimal paleothermometer $\alpha_{sea,T_c}$ in iCESM

In light of the USE discussed in section 3 and the inversion temperature responses discussed in section 2c, we propose that the optimal paleothermometer for surface temperature is

the seasonal inversion temperature slope:  $\alpha_{sea,T_c}$ . Indeed, given the inversion temperature response  $\Delta T_c/\Delta T_s \approx 1$  during deglaciation in (2.4) and the comparable  $\alpha_{sea,T_c}$  and  $\alpha_{deg,T_c}$  in (3.23), we have the scaling

$$\alpha_{sea,T_c} \approx \alpha_{deg,T_c} \approx \alpha_{deg,T_c} \times \Delta T_c/\Delta T_s \approx \alpha_{deg,T_s}; \quad (4.1)$$

Suggesting that  $\alpha_{sea,T_c}$  is a good surrogate for  $\alpha_{deg,T_s}$  in general. This is confirmed by comparing  $\alpha_{sea,T_c}$  in the iCESM using the  $\alpha_{sea,T_c}$  of PI simulation against the true paleothermometer  $\alpha_{deg,T_s}$  across Antarctica in the scatter diagram Fig. 9c (red dots). The Antarctic-mean (yellow plus) and regional scatters of  $\alpha_{sea,T_c}$  fall largely on the diagonal one-to-one line, suggesting a good representation of  $\alpha_{deg,T_s}$  for both the mean and spatial variability across Antarctica. A similar result can be seen in the reconstructed deglacial surface temperature change by applying a paleothermometer  $\alpha$  on LGM-PI  $\Delta\delta^{18}\text{O}$  as  $\Delta T_{rec} = \Delta\delta^{18}\text{O}/\alpha$ . The error of the  $\Delta T_{rec}$  by  $\alpha_{sea,T_c}$  is modest without systematic error (Fig. 9g). Note, however, the seasonal  $T_s$  slope  $\alpha_{sea,T_s}$  is too small to serve as a paleothermometer (Schneider et al.



2005; Stenni et al. 2016), because the small seasonal  $\Delta T_c/\Delta T_s$  response reduces  $\alpha_{\text{sea},T_s}$  from  $\alpha_{\text{sea},T_c}$  by  $\sim 50\%$  in iCESM and observations available (Fig. 4f; van Ommen and Morgan 1997; Schneider et al. 2005; Motoyama et al. 2005).

The new paleothermometer  $\alpha_{\text{sea},T_c}$  is superior to the traditional paleothermometer  $\alpha_{s,T_s}$  because  $\alpha_{\text{sea},T_c}$  represents the physical mechanism more correctly and therefore is more accurate and more robust. The accuracy of  $\alpha_{\text{sea},T_c}$  and the PI  $\alpha_{s,T_s}$  can be compared against the truth  $\alpha_{\text{deg},T_s}$  over Antarctica (Fig. 9a, versus Fig. 9c, red dots). The RMSE of  $\alpha_{s,T_s}$  is  $0.38\text{‰ K}^{-1}$ , more than twice that of  $\alpha_{\text{sea},T_c}$ , with a much greater spatial variability as indicated by the greater scatter from the diagonal line. Similarly, the error of the reconstructed temperature change  $\Delta T_{\text{rec}}$  by the PI  $\alpha_{s,T_s}$  is also larger (Fig. 9d), with the RMSE ( $\sim 6^\circ\text{C}$ ) about 3 times that based on PI  $\alpha_{\text{sea},T_c}$ . As another sensitivity test, if the slopes are derived from the LGM state, the RMSE of  $\alpha_{\text{sea},T_c}$  remains low as  $0.14\text{‰ K}^{-1}$  with a modest spread or spatial variability (Fig. 9c, blue dots), similar to that of PI. In contrast, the RMSE of LGM  $\alpha_{s,T_s}$  is almost doubled to  $0.57\text{‰ K}^{-1}$ , due to a larger spread (Fig. 9a, blue dots).

The robustness of  $\alpha_{\text{sea},T_c}$  originates partly from the fact that it only uses local measurements through time, rather than regional conditions that vary in space. In comparison, spatial slope  $\alpha_{s,T_s}$  has one intrinsic uncertainty: the domain choice for regression (Masson-Delmotte et al. 2008). A smaller domain resolves regional spatial variability better, but increases sampling error because of a reduced sample size, and vice versa. This introduces additional uncertainty as a paleothermometer, because the observed  $\alpha_{s,T_s}$  range widely from  $\sim 0.5\text{‰}$  to  $\sim 1.2\text{‰ K}^{-1}$  across Antarctica (Masson-Delmotte et al. 2008). The sensitivity of  $\alpha_{s,T_s}$  to domain size in observations can be seen in iCESM in Fig. 9 for  $\alpha_{s,T_s}$  calculated in three domain sizes:  $10^\circ \times 10^\circ$ ,  $40^\circ \times 40^\circ$ , and the entire Antarctica. With the three domain sizes, the error of  $\alpha_{s,T_s}$  remain large and less robust, relative to  $\alpha_{\text{sea},T_c}$ , for the slopes (Figs. 9a–c), and the predicted surface temperature changes of LGM-PI (Figs. 9d–g) over Antarctica. The large sensitivity of the spatial slope to domain size can be seen in observations in the 7 ice core sites in Fig. 10, where  $\alpha_{s,T_s}$  is calculated from the observation of Masson-Delmotte et al. (2008) as a function of domain sizes in spatial regression for each ice core (black squares). At the largest size (entire Antarctica),  $\alpha_{s,T_s}$  converges to the well-known value  $0.8\text{‰ K}^{-1}$  for all sites (Masson-Delmotte et al. 2008). For smaller domains around the ice core sites, however,  $\alpha_{s,T_s}$  can deviate substantially from  $0.8\text{‰ K}^{-1}$ . For example, around Dome C,  $\alpha_{s,T_s}$  increases rapidly from below  $0.5\text{‰}$  to  $\sim 1\text{‰ K}^{-1}$  when the domain radius increases from  $\sim 500$  to  $\sim 600$  km, with the correlation coefficient increases from  $\sim 0.5$  to over  $\sim 0.8$  (Fig. 10a, number of data points from 44 to 59). Finally, the larger error of  $\alpha_{s,T_s}$  than  $\alpha_{\text{sea},T_c}$  can also be seen in the predicted surface temperature changes during the deglacial evolution from 20 to 11 ka over the seven ice core sites as discussed in appendix F and Fig. F1.

#### b. Testing optimal paleothermometer $\alpha_{\text{sea},T_c}$ in observations

Our optimal paleothermometer  $\alpha_{\text{sea},T_c}$  can also be tested for real-world observations at Dome C using recent station

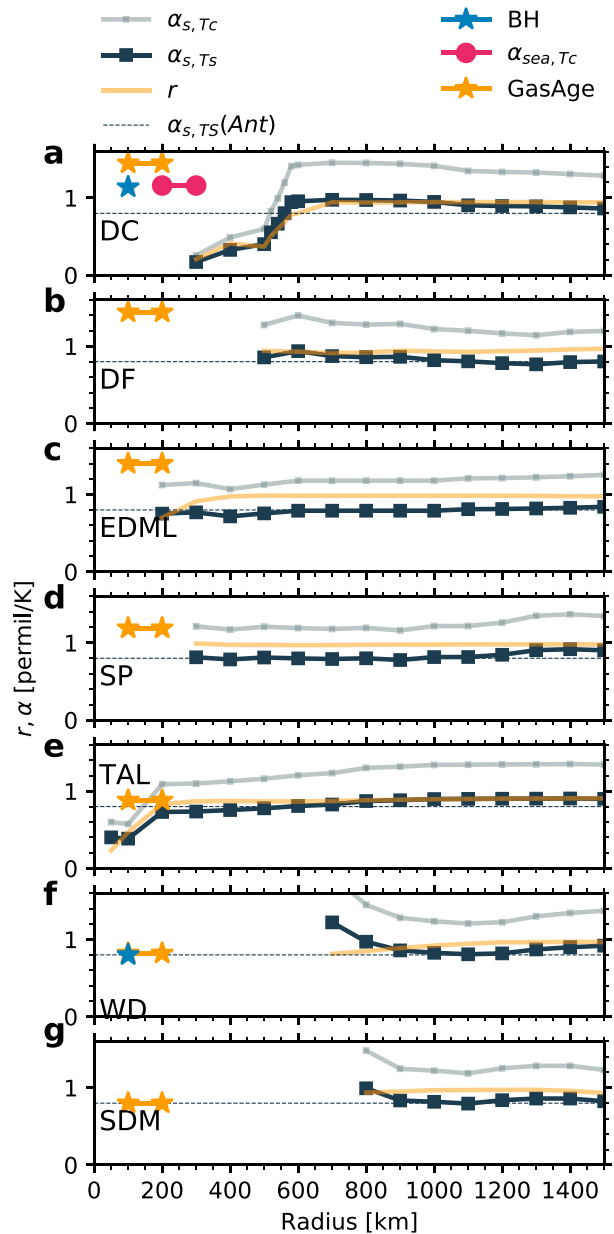


FIG. 10. Paleothermometers in the observation. (a) Spatial  $T_s$  slope  $\alpha_{s,T_s}$  derived from observations (Masson-Delmotte et al. 2008) within specified radius (km; black square) and entire Antarctic (dash) of Dome C, along with the correlation coefficient  $r$  (yellow) and upper bound  $\alpha_{s,T_c} = \alpha_{s,T_s}/0.67$  (gray solid), starting from the radius of more than 10 data points. (b)–(g) As in (a), but for Dome Fuji, EDML, South Pole, Talos Dome, West Antarctica, and Siple Dome, respectively. Yellow and blue [in (a) and (f)] stars are the  $\alpha_{\text{deg},T_s}$  reconstructions based on gas age–ice age and borehole thermometry, respectively (Buizert et al. 2021), while the red dot in (a) is the optimal paleothermometer of seasonal  $T_c$  slope  $\alpha_{\text{sea},T_c}$  (Stenni et al. 2016). Borehole thermometry  $\alpha_{\text{deg},T_s}$  for Dome Fuji ranges from 1 to 2.7 and is beyond the scale in (b).

observations and independent paleothermometers. Although there are no systematic observations of inversion temperatures and isotopes over most stations, Dome C has continuous observations on snow  $\delta^{18}\text{O}$  and radiosounding profiles from 2008 to 2010, providing a unique test for our theory. The monthly data on inversion temperature give a seasonal slope on  $T_c$  of  $1.16\text{‰ K}^{-1}$  (Stenni et al. 2016). Since monthly variability is dominated by the seasonal cycle, we can assume approximately  $\alpha_{\text{sea},T_c} \approx 1.16\text{‰ K}^{-1}$ . This  $\alpha_{\text{sea},T_c}$  is in good agreement with recent independent reconstructions of  $\alpha_{\text{deg},T_s}$  over Dome C as  $\alpha_{\text{deg},T_s} = 1.14\text{‰}$  and  $1.44\text{‰ K}^{-1}$ , based on gas age–ice age difference and borehole thermometry, respectively (Buizert et al. 2021) (black pluses in Fig. 9c; or compare red dots with yellow and blue stars in Fig. 10a). In comparison, the spatial  $T_s$  slope  $\alpha_{s,T_s}$  over Dome C is too small, which ranges from the earlier estimation  $0.75\text{‰ K}^{-1}$  (Lorius and Merlivat 1975), to the Antarctic domain average of  $0.8\text{‰ K}^{-1}$  and to less than  $\sim 1\text{‰ K}^{-1}$  for any domain size (Fig. 10a, also black pluses in Fig. 9a). The reported seasonal slope for surface temperature in Dome C of  $\alpha_{\text{sea},T_s} \approx 0.42\text{‰ K}^{-1}$  (Stenni et al. 2016) is also too small, due to the small inversion temperature response of  $\Delta T_c/\Delta T_s < 1$  in the seasonal cycle. Admittedly, two years of observational data is still limited in Dome C, which likely introduces uncertainties in modern-day observations of temperatures and isotopes and, in turn, in our estimation of  $\alpha_{\text{sea},T_s}$ . Nevertheless, our proposed  $\alpha_{\text{sea},T_c}$  seems to give an estimation of the paleothermometer  $\alpha_{\text{deg},T_s}$  sufficiently more accurately than the spatial slope  $\alpha_{s,T_s}$  such that our conclusion on the optimal paleothermometer  $\alpha_{\text{sea},T_c}$  over  $\alpha_{s,T_s}$  should be robust.

It is of interest to point out that, despite the deficiency of the spatial  $T_s$  slope  $\alpha_{s,T_s}$  as a paleothermometer, the spatial  $T_c$  slope  $\alpha_{s,T_c}$  may serve as an upper bound for paleothermometers for surface temperature  $T_s$ . Indeed, combining the inequality (3.24) derived from USE and the nearly neutral deglacial inversion response  $\Delta T_c/\Delta T_s \approx 1$  in (2.4), we have

$$\alpha_{s,T_c} > \alpha_{\text{deg},T_c} \approx \alpha_{\text{deg},T_c} \times \Delta T_c/\Delta T_s = \alpha_{\text{deg},T_s}. \quad (4.2)$$

This upper bound is difficult to test in observations because of the lack of extensive observations of inversion temperatures. Nevertheless, a crude estimation of  $\alpha_{s,T_c}$  may be made indirectly from the  $\alpha_{s,T_s}$  and the mean observed spatial inversion relation  $\Delta T_c/\Delta T_s = 0.67$  as

$$\alpha_{s,T_c} = \alpha_{s,T_s}/0.67, \quad (4.3)$$

for all of the seven sites (Fig. 10, gray lines). In comparison with independent estimations of  $\alpha_{\text{deg},T_s}$  values, this upper bound  $\alpha_{s,T_c}$  seems to hold across most sites (Fig. 10).

## 5. Conclusions

In this paper, we propose to understand the classical problem on  $\delta^{18}\text{O}$ –temperature paleothermometer in the unified framework of USE. First, in the general Rayleigh distillation process, our USE shows that both the spatial slope and temporal slope depend mainly on the Lagrangian slope  $\alpha_L$ . While

the spatial slope can be approximately represented by  $\alpha_L$ , the temporal slope is reduced significantly by the source temperature change, such that the temporal slope is smaller than the spatial slope in general, on inversion temperature  $T_c$ . Second, over the Antarctica, due to the weak inversion temperature changes across space relative to surface temperature changes and the comparable inversion temperature response during deglaciation with the surface temperature response, the spatial slope on surface temperature  $\alpha_{s,T_s}$  becomes comparable with the deglacial slope on surface temperature  $\alpha_{\text{deg},T_s}$ , accidentally, offering an explanation of this comparability previously found empirically in many modeling studies. Finally, USE suggests that the optimal paleothermometer should be the seasonal slope on inversion temperature  $\alpha_{\text{sea},T_c}$ , instead of the traditional spatial slope  $\alpha_{s,T_s}$ . This optimal paleothermometer is tested well in iCESM as well as in the observations available. The myriad relations among different slopes and the related inversion layer temperature responses are summarized in Fig. 5.

Therefore, we can address the fundamental questions raised in the introduction.

Question 1b: What is the relation among these different aforementioned isotope slopes in general? Temporal slope is in general smaller than the spatial slope in  $T_c$ .

Question 1a: Why does the spatial slope  $\alpha_{s,T_s}$  as a whole appear to be comparable with the deglacial slope  $\alpha_{\text{deg},T_s}$  over Antarctica? This is caused by a greater spatial slope than deglacial slope in  $T_c$  accidentally compensated by a smaller deglacial temperature response in inversion layer temperature relative to surface temperature  $\Delta T_c/\Delta T_s < 1$ .

Question 2: What slope is the most suitable for estimating past surface temperature change over the Antarctica? It is the seasonal slope on inversion layer temperature  $\alpha_{\text{sea},T_c}$ .

It is important to note that our new paleothermometer  $\alpha_{\text{sea},T_c}$  can be measured, in principle, in the present and future, and therefore offers the promise of more accurate reconstructions of past Antarctica temperature in the future. Much future work is, however, needed for coordinated and long-term monitoring program on isotope and temperature profiles over the ice core sites. These modern-day observations will provide much improved paleothermometer  $\alpha_{\text{sea},T_c}$  and the upper bound  $\alpha_{s,T_c}$ . More generally, the USE framework developed here clarifies the relationship among spatial and temporal slopes and provides a guideline for future estimations of paleothermometers over polar regions (Cuffey et al. 2016; Buizert et al. 2021) and, potentially, the tropics at high altitude (Thompson and Mosley-Thompson 2000).

*Acknowledgments.* We thank Drs. E. Mosley-Thompson, L. Thompson, D. Bromwich, D. Noone, J. Nussbaumer, and J. Severinghaus for helpful discussions. We are also grateful to two anonymous reviewers for careful review and constructive comments, which improved the presentation of the paper substantially. This work is supported by Laoshan Laboratory Project LSKJ202203300, U.S. NSF 2002506, 2002521, and 2019719 (the Center for Oldest Ice Exploration, an NSF Science and

Technology Center). The CESM project is supported primarily by the NSF. This material is based on work supported by the National Center for Atmospheric Research, which is a major facility sponsored by the NSF under Cooperative Agreement 1852977. Computing and data storage resources, including the Cheyenne supercomputer (DOI: [10.5065/D6RX99HX](https://doi.org/10.5065/D6RX99HX)), were provided by the Computational and Information Systems Laboratory (CISL) at NCAR.

**Data availability statement.** All model data supporting our findings are archived at <https://doi.org/10.5281/zenodo.5226271>. Paleoclimate proxy data are from NOAA (<https://www.ncdc.noaa.gov/data-access/paleoclimatology-data>), and temperature observations are from <https://www.ncei.noaa.gov/products/weather-balloon/integrated-global-radiosonde-archive>.

## APPENDIX A

### Weather Data Analysis

Radiosonde data for four interior Antarctic stations, including AMUNDSEN-SCOTT (South Pole), BYRDSTN (Byrd), CONCORDIA (Dome C), and VOSTOK (Vostok), are obtained from the NOAA public repository (<https://www.ncei.noaa.gov/products/weather-balloon/integrated-global-radiosonde-archive>). Among them, summer observations are provided twice daily at 0000 and 1200 UTC, while only 0000 UTC observations are available in winter. To avoid diurnal bias, we only employ the 0000 UTC observations, except at Dome C, where summer observations are only available at 1200 UTC. In Figs. 4a and 4c, we plot Dome C as “+” as a caveat of its difference from others.

Since the raw radiosounding data are on variable pressure levels, we linearly interpolate them to common pressure levels between 100 and 1000 hPa, with a vertical interval of 1 hPa. This fine interval is chosen to keep all raw data on the new levels. Afterward, we pick up the first layer in each vertical profile as the surface, which are near 600 and 700 hPa for the four stations. To compare with the model, the pressure coordinate in each profile is then converted into sigma coordinate by normalizing aloft pressure levels to the corresponding surface pressure  $p/p_s$ . Finally, the inversion layer is determined as the warmest layer in the sigma profile, which is near 0.9 as seen from Figs. 3a and 3b.

## APPENDIX B

### Inversion Layer Responses to Different Climate Forcings

Here, we discuss the inversion layer temperature response in more details. First, we note that the larger deglacial response of inversion temperature in (2.4) is a robust feature across models. We also calculated the temperature responses in the inversion layer (approximately) and surface layer over the Antarctic in the 6 PMIP3 experiments ([esgf-node.llnl.gov/projects/esgf-llnl](https://esgf-node.llnl.gov/projects/esgf-llnl), [pmip3.lscce.ipsl.fr](https://pmip3.lscce.ipsl.fr)): CCSM4, MPI-ESM-P, GISS-E2\_R, IPSL-CM5A-LR, MIROC-ES, and MRI-CGCM3 (Braconnot et al. 2011, 2012). All the six models show that the Antarctica  $\Delta T_c/\Delta T_s$  for spatial changes (red) are

consistently smaller than their deglacial changes (black) (Fig. B1a). The uncertainty associated with the cross-model spread can be seen smaller than the difference between different slopes. Note that, in PMIP models, while surface air temperatures are stored in separate files, temperatures in the air column are stored after the interpolation onto standard pressure levels all the way to sea level (including fake temperatures below ice topography!). Therefore, the near-surface inversion layer is severely distorted. As such, the 600-hPa level is selected as a proxy of the inversion layer temperature because this level is just above the Antarctic Plateau and is therefore little distorted after the interpolation (Buizert et al. 2021). In all other models discussed, model outputs are all stored in the original topography-following sigma level. Therefore, the temperature profiles in the original sigma-hybrid level are presented to best preserve the surface inversion layer structure.

Second, this robust difference in inversion layer responses is not caused simply by the difference between spatial and temporal changes. Indeed, the seasonal change, albeit a temporal change, also shows a small inversion temperature change similar to the spatial change, but different from the deglacial temporal change as seen in iCESM, where  $\Delta T_c/\Delta T_s < 0.5$  as seen in the scatter diagram Fig. 4c and vertical profiles (DJF–JJA, Figs. 3e,f,h), as well as the PMIP models (Fig. B1a, blue dots) and the present weather station observations (Fig. 4c, black marks; Connolley 1996).

The different inversion layer responses between the small spatial/seasonal changes and larger deglacial change, we hypothesize, are caused by different physical mechanisms. The rapidly diminishing solar radiation toward polar region, especially in winter, leads to a much stronger cooling in the surface than in the lower troposphere, or seasonal  $\Delta T_c/\Delta T_s < 1$ , corresponding to an intensified inversion layer, as seen in the scatter diagram (Fig. 4c) and spatial map (Figs. B1e,b) in comparison of  $\Delta T_c$  with  $\Delta T_s$ . This seasonal response is the strongest toward Antarctic interior, especially in winter as seen in the vertical profiles in Figs. 3e, 3f, and 3h. In contrast, the large  $T_c$  response of  $\Delta T_c/\Delta T_s \sim 1$  during deglaciation, we hypothesize, is forced by long-term greenhouse gas (GHG) forcing, which heats the atmosphere downward in longwave radiation. Over polar regions, this downward heating is further amplified by the heat transport from lower latitude via the dynamic GHG-plus feedback (Cai 2006; Lu and Cai 2010). The long-term GHG forcing can also induce sea ice feedback and, in turn, larger surface temperature change over the Southern Ocean than over the Antarctica as seen in the temperature responses in the surface (Fig. B2d). This larger temperature change over Southern Ocean could then affect the lower troposphere over Antarctica Plateau via synoptic atmospheric mixing (Fig. B2a) (Noone 2008). If our hypothesis is correct, we should also expect a greater  $T_c$  response to GHG in global warming experiments than that to seasonal/spatial changes. This is indeed confirmed in our model (Fig. B1b) and other models, including CCSM4 (Fig. B1c) and GFDL SPEAR (Fig. B1d).

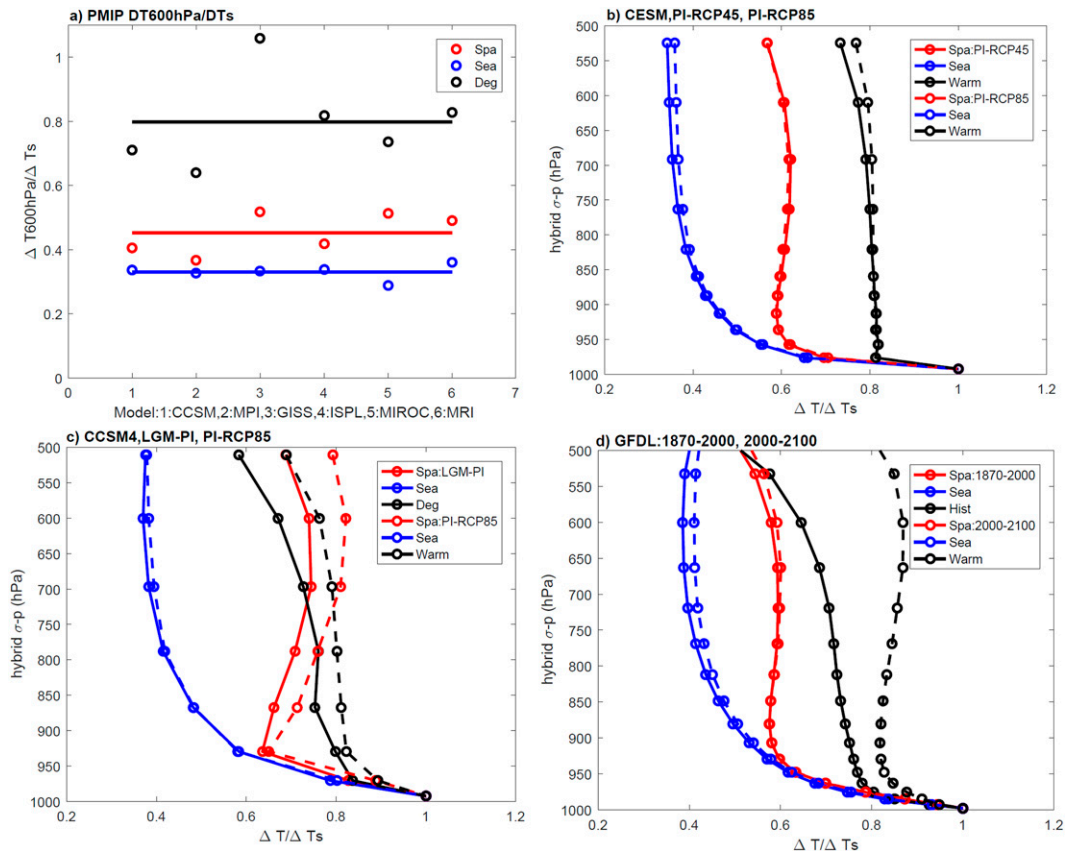


FIG. B1. Inversion layer temperature changes (spatial, seasonal, and climate change) across models over Antarctica. (a) LGM to PI changes in PMIP3 models ([esgf-node.llnl.gov/projects/esgf-llnl](https://esgf-node.llnl.gov/projects/esgf-llnl), [pmip3.lscce.ipsl.fr](https://pmip3.lscce.ipsl.fr)) compared with spatial and seasonal changes similar to Fig. 3h, but only for the 600-hPa level, in model 1 (CCSM4), 2 (MPI-ESM-P), 3 (GISS-E2\_R), 4 (IPSL-CM5A-LR), 5 (MIROC-ES), and 6 (MRI-CGCM3), with the cross-model ensemble means in solid lines. (b) As in Fig. 3h, but for two global warming scenarios (RCP45, solid; RCP85, dash) in CESM1. Vertical profiles of the temperature differences for spatial difference (red), seasonal difference (blue), and global warming changes (black, between 1981–2000 and 2080–2100 averages), with each profile normalized by its surface temperature change  $\Delta T_s$ . (c) As in (b), but in CCSM4 for two scenarios of climate changes between LGM and PI (solid) and between PI and RCP85 (dash). (d) As in (b) and (c), but for GFDL model (SPEAR-LO; [Delworth et al. 2020](#)) in the Large Ensemble (5-member ensemble mean) Historical and RCP85 ([Lu et al. 2020](#)) for two periods of climate changes of 1850–70 to 1980–2000 (solid) and 1980–2000 to 2180–2100 (dash). In (b)–(d), data are on the native hybrid sigma-pressure levels. In all the panels, the normalized inversion temperatures are 0.8–0.9 for climate change,  $\sim 0.6$  for spatial difference, and  $\sim 0.4$ –0.5 for seasonal difference, consistent with iCESM in Fig. 3h. Note that, in PMIP models, temperature at the normal pressure level of 600 hPa is selected as a proxy of the inversion layer temperature because this level is just above the Antarctic Plateau and is little distorted after the interpolation. In all other models, data are all stored and therefore presented in the original topography-following sigma level.

## APPENDIX C

### Tagging Experiments

Two water tagging experiments are carried out at the LGM (20 ka) and PI (0 ka) in the atmospheric component model iCAM5.3 ([He et al. 2021a](#)). The LGM and PI tagging experiments are forced by the sea ice distribution, sea surface temperature, and sea surface  $\delta^{18}\text{O}$  and  $\delta D$  extracted from the iTRACE experiment as well as the continental ice sheets, orbital parameters, and GHG concentration at 20 ka and a preindustrial control simulation, respectively. Each tagging experiment is integrated for 40 years with the last

20 years used for analysis. In the tagging experiments, the life cycle of  $\text{H}_2^{16}\text{O}$  (vapor) and  $\text{H}_2^{18}\text{O}$  (vapor) are tracked from each tagging region (source region) where they evaporate and then follow the hydrological processes in the model to the region where they rain out (sink region). The global source regions are divided into 25 subregions, with 12 covering the land and 13 covering the ocean (Figs. B2a,b). The moisture source to the Antarctica is overwhelmingly from the Southern Hemisphere oceans for both PI and LGM and in both winter and summer. The dominant contribution to Antarctica is from the Southern Ocean (>50%), followed by southern South Pacific, south Indian Ocean, and South



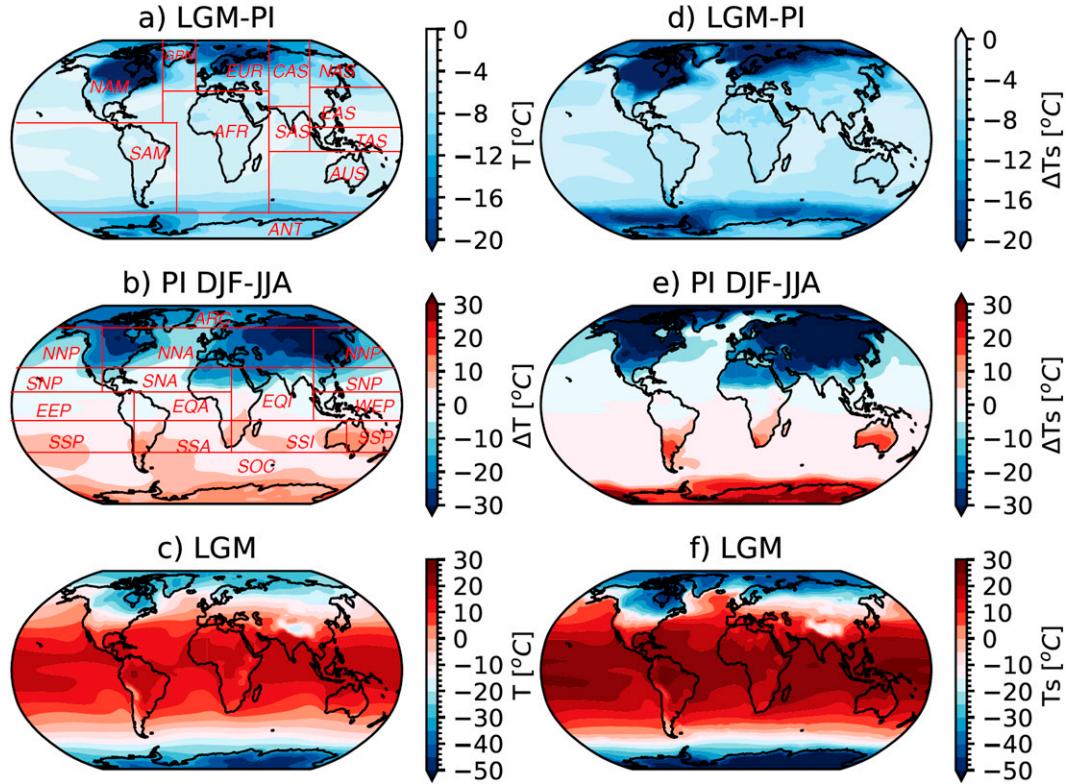


FIG. B2. Global distribution of temperature and their differences at the surface and inversion layer in iCESM. Difference inversion layer annual-mean temperature difference  $\Delta T_c$  for (a) deglacial change (LGM – PI) and (b) seasonal difference (DJF – JJA) in PI. (c) Inversion layer temperature  $T_c$  at LGM. (d)–(f) As in (a)–(c), but for surface air temperature  $T_s$ . In (a) and (b), the red boxes delineate the 12 and 13 tagging regions over land and ocean, respectively.

Atlantic, with the first four sources from the Southern Hemisphere oceans accounting for over 90% of the total source (as shown in Figs. E1a4 and E1b4), consistent with other tagging experiments (e.g., Markle et al. 2017; Bailey et al. 2019).

#### APPENDIX D

##### USE Decomposition

The differential forms of USE spatial and temporal Eqs. (3.12) and (3.14) are valid for infinitesimal changes. For practical application to finite changes, it is useful to derive an approximate USE decomposition.

##### a. Spatial slope decomposition

For spatial slope, we apply the isotope Eq. (3.11) to two regions of equal area (but not necessarily continuous in space) denoted as “N” and “S” regions,

$$\delta_N \equiv \delta(x_N, t) = \sum_{i=1}^n \delta_{Ni} w_{Ni} + \delta_d(t), \quad (\text{D.1a})$$

$$\delta_S \equiv \delta(x_S, t) = \sum_{i=1}^n \delta_{Si} w_{Si} + \delta_d(t), \quad (\text{D.1b})$$

where  $\delta_{Ni} \equiv \delta_i(x_N, t)$ ,  $w_{Ni} \equiv w_i(x_N, t)$ , and  $\delta_{Si} \equiv \delta_i(x_S, t)$ ,  $w_{Si} \equiv w_i(x_S, t)$  are the contribution from individual sources obtained from tagging experiments. The spatial slope can therefore be derived similar to (3.12) in the central difference scheme as

$$\alpha_s(x, t) \equiv \frac{\delta_N - \delta_S}{T_N - T_S} = \alpha_{Ls} + \sum_{i=1}^n \bar{\delta}_i \frac{w_{Ni} - w_{Si}}{T_N - T_S}, \quad (\text{D.2})$$

where

$$\alpha_{Ls} = \sum_{i=1}^n \alpha_{Ls,i} \bar{w}_i, \quad \text{and} \quad \alpha_{Ls,i} \equiv \frac{\delta_{Ni} - \delta_{Si}}{T_N - T_S}, \quad (\text{D.3})$$

are, respectively, the total and individual source contribution to, the discrete Lagrangian slope for spatial slope. Additionally,  $T_N \equiv T(x_N, t)$ ,  $T_S \equiv T(x_S, t)$  are the averaged temperatures of the N and S regions, respectively, and

$$\bar{w}_i = \frac{w_{Ni} + w_{Si}}{2}, \quad \text{and} \quad \bar{\delta}_i = \frac{\delta_{Ni} + \delta_{Si}}{2}. \quad (\text{D.4})$$

Note that the spatial decomposition (D.2)–(D.4) can be applied directly to the analysis of a climate model simulation, because they only use the values of  $\delta_i$ , instead of the Lagrangian



isotope function  $L(T, T_0)$  in (3.3) or (3.10). It should also be noted that,  $\alpha_{Ls,i}$  in (D.3) may differ for different sources slightly because of the finite change, especially for large regions, unlike the case of infinitesimal change, where  $\alpha_L$  is independent of sources as derived from (3.8) and (3.9).

*b. Temporal slope decomposition*

For the temporal slope, there are two approaches. The “bottom-up” approach uses an analog theoretical model for decomposition and requires explicitly the Lagrangian isotope function  $L(T, T_0)$ . The “top-down” approach applies directly to a climate model output, in which  $L(T, T_0)$  is assumed implicitly.

1) BOTTOM-UP APPROACH WITH  $L(T, T_0)$

We first assume  $L(T, T_0)$  is known as in (3.3) for a generalized Rayleigh process (3.1). For the temporal slope between times  $t_p$  and  $t_q$ , we have from Eqs. (3.10) and (3.11):

$$\begin{aligned} \delta_p &\equiv \delta(x, t_p) = \sum_{i=1}^n \delta_{pi} w_{pi} + \delta_{dp} \\ &= \sum_{i=1}^n L(T_p, T_{0i,p}) w_i(x, t_p) + \delta_d(t_p), \end{aligned} \tag{D.5a}$$

$$\begin{aligned} \delta_q &\equiv \delta(x, t_q) = \sum_{i=1}^n \delta_{qi} w_{qi} + \delta_{dq} \\ &= \sum_{i=1}^n L(T_q, T_{0i,q}) w_i(x, t_q) + \delta_d(t_q), \end{aligned} \tag{D.5b}$$

where  $T_p \equiv T(x, t_p)$ ,  $T_q \equiv T(x, t_q)$  are from the output of the forward model simulation and

$$\begin{aligned} T_{0i,p} &\equiv T_{0i}(x, t_p), \quad T_{0i,q} \equiv T_{0i}(x, t_q), \\ \delta_{pi} &= \delta_i(x, t_p) = L(T_p, T_{0i,p}), \quad \delta_{qi} = \delta_i(x, t_q) = L(T_q, T_{0i,q}), \end{aligned} \tag{D.5c}$$

are derived from the tagging experiment. A temporal slope can therefore be derived analogous to the USE Eq. (3.14) as

$$\begin{aligned} \alpha_t(x, t) &\equiv \frac{\delta_p - \delta_q}{T_p - T_q} = \alpha_{Lt} - \frac{\sum_{i=1}^n \bar{w}_i \alpha_{Lo,i} (T_{0i,p} - T_{0i,q})}{T_p - T_q} \\ &\quad + \frac{\sum_{i=1}^n \bar{\delta}_i (w_{i,p} - w_{i,q})}{T_p - T_q} + \frac{\delta_{dp} - \delta_{dq}}{T_p - T_q}, \end{aligned} \tag{D.6}$$

where

$$\begin{aligned} \alpha_{Lt} &= \sum_{i=1}^n \bar{w}_i \alpha_{Lt,i} \quad \text{and} \\ \alpha_{Lo,i} &\equiv \frac{1}{2} \left\{ \frac{L(T_p, T_{0i,p}) - L(T_q, T_{0i,p})}{T_p - T_q} \right. \\ &\quad \left. + \frac{L(T_p, T_{0i,q}) - L(T_q, T_{0i,q})}{T_p - T_q} \right\} \end{aligned} \tag{D.7}$$

are, respectively, the total and individual source discrete Lagrangian slope for temporal slope,

$$\bar{w}_i = \frac{w_{pi} + w_{qi}}{2}, \quad \text{and} \quad \bar{\delta}_i = \frac{\delta_{pi} + \delta_{qi}}{2}, \tag{D.8}$$

and

$$\begin{aligned} \alpha_{Lo,i} &= \frac{1}{2} \left\{ \frac{L(T_{0i,p}, T_q) - L(T_{0i,q}, T_q)}{T_{0i,p} - T_{0i,q}} \right. \\ &\quad \left. + \frac{L(T_{0i,p}, T_p) - L(T_{0i,q}, T_p)}{T_{0i,p} - T_{0i,q}} \right\} \end{aligned} \tag{D.9}$$

is the Lagrangian slope with respect to the source temperature, where we have used, from (3.5),  $L(T, T_0) = -L(T_0, T)$ . Equations (D.6)–(D.9) give “bottom-up” USE decomposition for temporal slope. Note that, due to the finite change, the total Lagrangian slope for spatial slope  $\alpha_{Ls}$  in Eq. (D.3) is usually not exactly the same as that for the temporal slope  $\alpha_{Lt}$  in Eq. (D.7), especially for larger regions. In our approximate Rayleigh model (3.4), due to the use of central value approximation,  $d\delta/dT = \alpha$  is no longer strictly a function of  $T$  only. Thus, even in the differential form, (3.3) is no longer strictly valid. This also contributes to a small difference between  $\alpha_{Ls}$  and  $\alpha_{Lt}$ . However, this approximation does not affect our major conclusions qualitatively.

2) TOP-DOWN APPROACH WITHOUT  $L(T_p, T_0)$

In a climate model simulation,  $L(T_p, T_0)$  is unknown even if it may exist. This makes (D.7) and (D.9) infeasible. We can nevertheless use a top-down approach that substitutes the Lagrangian slope for temporal slope with that for spatial slope, because these two Lagrangian slopes are identical in the differential form (3.13) and (3.15) for infinitesimal changes in generalized Rayleigh processes. That is, (D.7) is replaced with

$$\alpha_{Lt} = \alpha_{Lo,i} = \alpha_{Ls}, \tag{D.10}$$

with  $\alpha_{Ls}$  estimated from (D.3). Additionally, since from (3.3), we have approximately

$$\Delta L \approx a(T) \Delta T - \alpha_{Lo}(T_0) \Delta T_0. \tag{D.11}$$

Instead of using (D.9), we now estimate  $\alpha_{Lo,i}$  from (D.11) and (D.5c) as a residual as

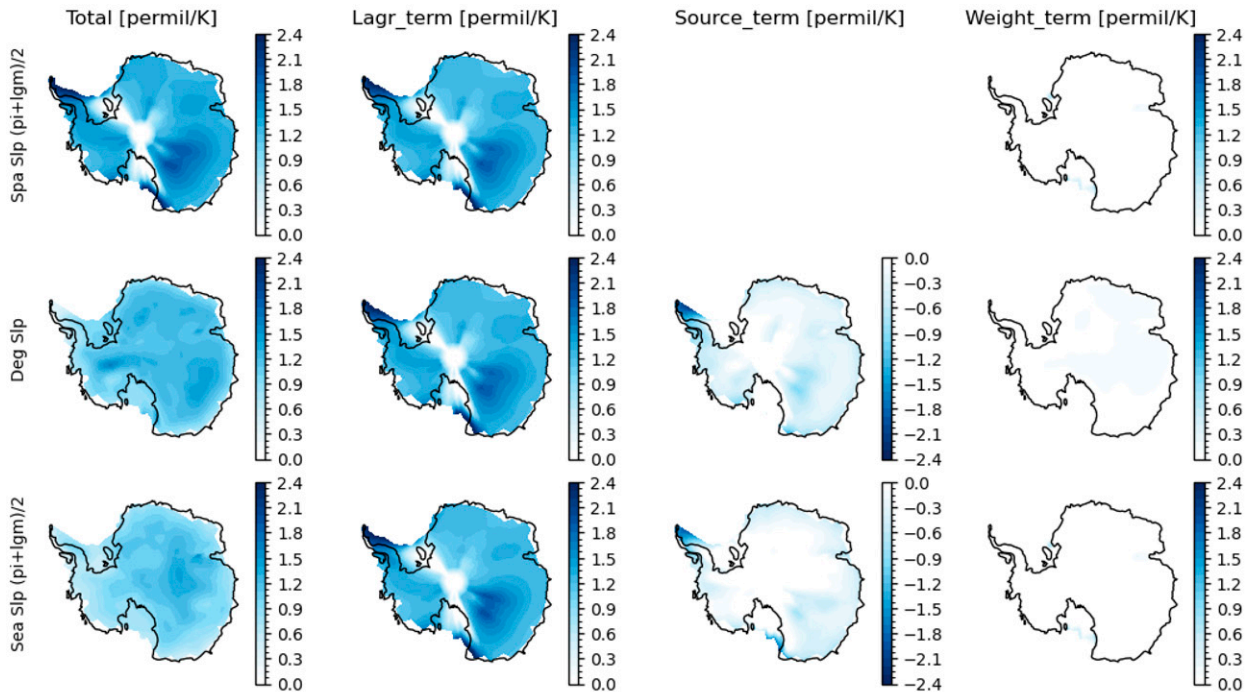
$$\alpha_{Lo,i} = \frac{\alpha_{Lt}(T_p - T_q) - (\delta_{pi} - \delta_{qi})}{T_{0i,p} - T_{0i,q}}. \tag{D.12}$$

The top-down decomposition equations are therefore (D.6), (D.10), (D.8), and (D.12).

An example of the decompositions of spatial and deglacial slopes for the Antarctica are given in Fig. D1.

A comparison of the two methods shows some robust features. First, the source term (column 3) is smaller than the Lagrangian term, but not negligible, leading to the reduced deglacial and seasonal slope from Lagrangian slope. Second, the weight term is negligible. We also note that the Lagrangian slope is the largest (column 2) and tends to be

## a) Top-down scheme in iCESM



## b) Bottom-up scheme in Rayleigh model

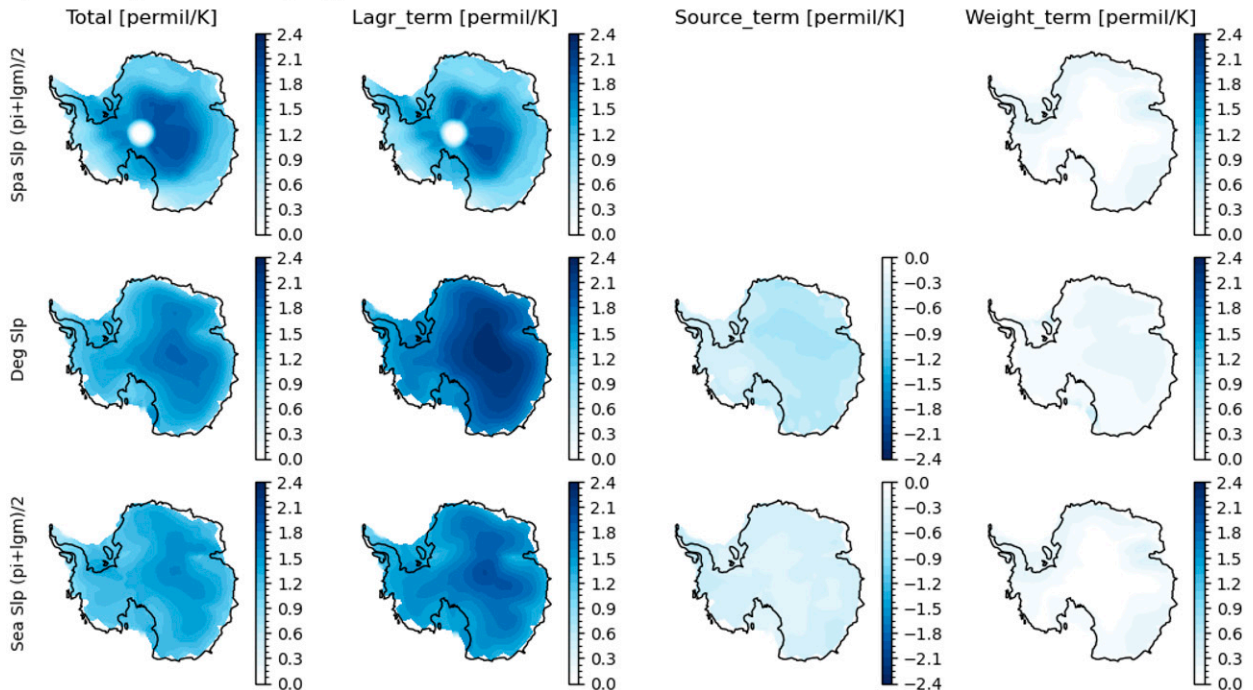


FIG. D1. USE decompositions of spatial, deglacial, and seasonal slopes using two schemes (see appendix C for details). (a) Decomposition using the “top-down” scheme in iCESM. From top to bottom are spatial, deglacial, and seasonal slopes, with the total slope, Lagrangian slope, source, and weight change terms in the four columns (labeled at the top). (b) As in (a), but for the “bottom-up” scheme using the Rayleigh model (the  $\delta^{18}\text{O}$  in Fig. 7). Note the color map for the source term is of the opposite sign to others. For the deglacial slope, the ice volume term is not shown as it is a uniform response in the Antarctica with a value of  $\sim 0.1\text{‰ K}^{-1}$ . The spatial slope is calculated in each  $10^\circ \times 10^\circ$  box using the top 1/3 minus bottom 1/3 points. The seasonal and spatial slopes are the average between LGM and PI.



FIG. E1. Testing source sensitivity on deglacial and seasonal slopes in Rayleigh model. (a) Deglacial slope derived using different source schemes as functions of the sources (labeled at the bottom panel in the order of decreasing weight). (a1) Deglacial slope and its components (see legend) in the single source scheme: each source is treated as the only source (weight set to 1). (a2) As in (a1), but for the 2 sources: the world sources consist of this source and the other source that combines the rest of the 24 sources. (a3) As in (a1), but for the accumulative source scheme: the contribution from each source is added accumulatively in the order of the source weight as in the convention reconstruction using the Rayleigh model. (a4) The weight of each source (for region see Figs. B2a,b) in decreasing weight order. (a5) Source temperature and (a6) its change (PI-LGM) of each source (average over the tagged region). (b1)–(b6) As in (a1)–(a6), but for the seasonal slope at PI. In (a3) and (b3), the slopes almost converge to the final value after the first five sources are included, because their weights account for more than 99% of the total weights, as shown in (a4) and (b4).

comparable to the spatial slope (first row in Figs. D1a,b), but greater than the deglacial (second row) and seasonal (third row) slopes. Note, however, this feature is by construction in the top-down approach, in which the Lagrangian slope is taken to be equal to the spatial slope. Also, by construction, in the finite difference case here, the Lagrangian slopes are different in the bottom-up scheme for spatial, deglacial and seasonal slopes, but the same in the top-down scheme.

## APPENDIX E

### Source Sensitivity

Given the arbitrariness of the schemes of source regions in general, we will show, in the application of USE to our Rayleigh model, that the temporal slope is not very sensitive to the source details. We first test the sensitivity of  $\alpha_{\text{deg},T}$  to different schemes of the sources in Fig. E1a. The weight  $w_i$  and the source temperature  $T_{oi}$  of PI and LGM



are shown in Fig. E1a4, while the deglacial change of each source temperature  $\Delta T_{oi}$  (PI-LGM) is shown in Fig. E1a6. As discussed before, the major sources are from the Southern Hemisphere oceans (the leading five sources), their climatology temperature are  $\sim 30^\circ\text{C}$  colder than that of Antarctica (the first five versus the sixth bar in Fig. E1a5), and their temperature changes are comparable or smaller than that over Antarctica (the first five versus the sixth bars in Fig. E1a6).

#### a. Scheme 1: A single source scheme

In this scheme, we assume that each source is the sole source to the deglacial change by setting its weight as 1, while keeping its source temperature response  $\partial T_{oi}$  unchanged as in the tagging experiment. Fig. E1a1 shows the four terms in USE temporal slope Eq. (3.14) [as decomposed using the “bottom-up” scheme (D.6)–(D.9)] as a function of different sources. It is seen that for almost all the sources, the slope is always dominated by  $\alpha_L$  of about the same magnitude (blue), which is reduced substantially by the source temperature term (red) to the final deglacial slope  $\alpha_{\text{deg},T}$  (yellow). The weight change term is identically zero in this case.

#### b. Scheme 2: Two-source scheme

Now, we assume the moisture sources over the world consist of two regions only. We chose one source and combine the rest sources as the other source. The variations of the four terms with the source again show little sensitivity (Fig. E1a2). Again, the  $\alpha_{\text{deg},T}$  is dominated by  $\alpha_L$ , reduced substantially by the source term, but little affected by the weight change term.

#### c. Scheme 3: Accumulative sources

Now, we add the contribution of each source successively in the order of its weight (Fig. E1a4). It is seen that the four terms and the final  $\alpha_{\text{deg},T}$  almost reaches the saturation after the incorporation of the leading five sources, all of which are from Southern Hemisphere oceans. This confirms the importance of the dominant moisture contribution from the Southern Hemisphere oceans.

The insensitivity can also be understood from a scaling analysis. Assuming a cooling magnitude comparable in the sources and the Antarctica  $\partial T_{oi} \sim \partial T_c$ , and a climatological mean source temperature  $T_0 \sim -10^\circ\text{C}$  (mainly over the midlatitude Southern Ocean; Markle et al. 2017) and Antarctic temperature  $T_c \sim -30^\circ\text{C}$  (Fig. 6c), we have a source reduction of  $\alpha_L(T_{0i})/\alpha_L(T_c) \sim 30\%$  (Fig. 6c), comparable with the USE decompositions (Figs. D1a,b, source term compared with  $\alpha_L$  term for deglaciation).

Similarly, we can test the sensitivity of the PI seasonal slope  $\alpha_{\text{sea},T}$  to different schemes of the sources (Fig. E1b), the only difference is to replace the warm/cold climate states from PI/LGM to DJF/JJA for PI. In particular, one notes that the source temperature changes are all of the same sign as the Antarctica for the dominant sources in the Southern Hemisphere, as shown in Fig. E1b6 (the first five versus the sixth). This is qualitatively similar to that of

deglacial change Fig. E1a6, giving a physical base for using the seasonal slope for deglacial slope as a paleothermometer.

## APPENDIX F

### Comparison of $\alpha_{\text{sea},T_c}$ and $\alpha_{s,T_s}$ in iCESM

In iCESM, our default domain for spatial slope is the  $10^\circ \times 10^\circ$  domain. Given our model resolution of  $\sim 2^\circ \times 2^\circ$ , this domain contains  $\sim 25$  grid points. As discussed earlier, the PI  $\alpha_{s,T_s}$  thus derived scatter widely between  $0.5\%$  and  $1.5\%$   $\text{K}^{-1}$  (over 90% points in Fig. 9a, red dots), roughly comparable with the spread in the observation (although the observation has a much higher spatial resolution) (Masson-Delmotte et al. 2008). With the domain expanded to  $40^\circ \times 40^\circ$  (of  $\sim 320$  grid points), the spread is reduced substantially as seen in the scatter (Fig. 9b, red dots). However, the slopes are now aligned predominantly in the vertical, instead of diagonal, implying that  $\alpha_{s,T_s}$  is too uniform to resolve the spatial variability of the true model  $\alpha_{\text{deg},T_s}$ . The RMSE of  $\alpha_{s,T_s}$  relative to  $\alpha_{\text{deg},T_s}$  remains large ( $0.44\%$   $\text{K}^{-1}$ ), due mainly to a systematically smaller mean slope (yellow plus). This smaller  $\alpha_{s,T_s}$  leads to an overestimation of the deglacial cooling over the entire Antarctica, such that the RMSE of reconstructed  $\Delta T_{\text{rec}}$  still remains high ( $4.7^\circ\text{C}$ , Fig. 9e). When the regression domain is expanded to the entire Antarctica, there is only a single PI  $\alpha_{s,T_s} = 0.98\%$   $\text{K}^{-1}$ , so the spatial variability is completely lost (solid vertical line in Fig. 9b). The absence of spatial variability leads to a systematically smaller (larger)  $\alpha_{s,T_s}$  and, in turn, overestimation (underestimation) of the cooling over the most of the interior Antarctica Plateau (coastal region) (Fig. 9f), where the true  $\alpha_{\text{deg},T_s}$  is large (small) due to the colder (warmer) temperature (not shown). In PI, the absence of spread appears to reduce the RMSE to  $\sim 0.2\%$   $\text{K}^{-1}$  for  $\alpha_{s,T_s}$  and to  $\sim 2^\circ\text{C}$  for  $\Delta T_{\text{rec}}$ . However, the reduction of RMSE using the Antarctic mean seems to be a coincident in the PI state. At LGM, if the domain expands first from  $10^\circ \times 10^\circ$  to  $40^\circ \times 40^\circ$  and then to the entire Antarctica (of  $\alpha_{s,T_s} = 1.13\%$   $\text{K}^{-1}$ , dash black line in Fig. 9b), the RMSEs of  $\alpha_{s,T_s}$  and  $\Delta T_{\text{rec}}$  first decrease by 50% to  $0.22\%$   $\text{K}^{-1}$  and  $2.2^\circ\text{C}$ , but then increase by 50% to  $0.27\%$   $\text{K}^{-1}$  and  $3.2^\circ\text{C}$ , respectively.

The accuracy and robustness of the paleothermometer  $\alpha_{\text{sea},T_c}$  over  $\alpha_{s,T_s}$  can also be seen in comparing the surface temperature reconstructions for the entire deglacial evolution (20–11 ka) in iCESM. The RMSE maps over Antarctica remain similar to those for LGM-PI in Figs. 9d–g (not shown). Figure F1a shows examples of time series of surface temperature reconstructions for five Antarctica core sites. It is seen that, overall, the  $\alpha_{\text{sea},T_c}$  reconstructions are more accurate while the  $\alpha_{s,T_s}$  reconstructions vary substantially for different domain sizes. Averaged across the five core sites and for the entire period of 20 to 11 ka, the RMSEs of the reconstructed temperatures are  $0.93^\circ\text{C}$  for  $\alpha_{\text{sea},T_c}$ , but  $1.3^\circ$ ,  $1.6^\circ$ , and  $1.7^\circ\text{C}$  for the PI  $\alpha_{s,T_s}$  values of the domains of  $10^\circ \times 10^\circ$ ,  $40^\circ \times 40^\circ$ , and Antarctica, respectively.

The sensitivity of  $\alpha_{s,T_s}$  to domain size can also be seen if we use our model slopes on the observed  $\delta^{18}\text{O}$  over seven ice

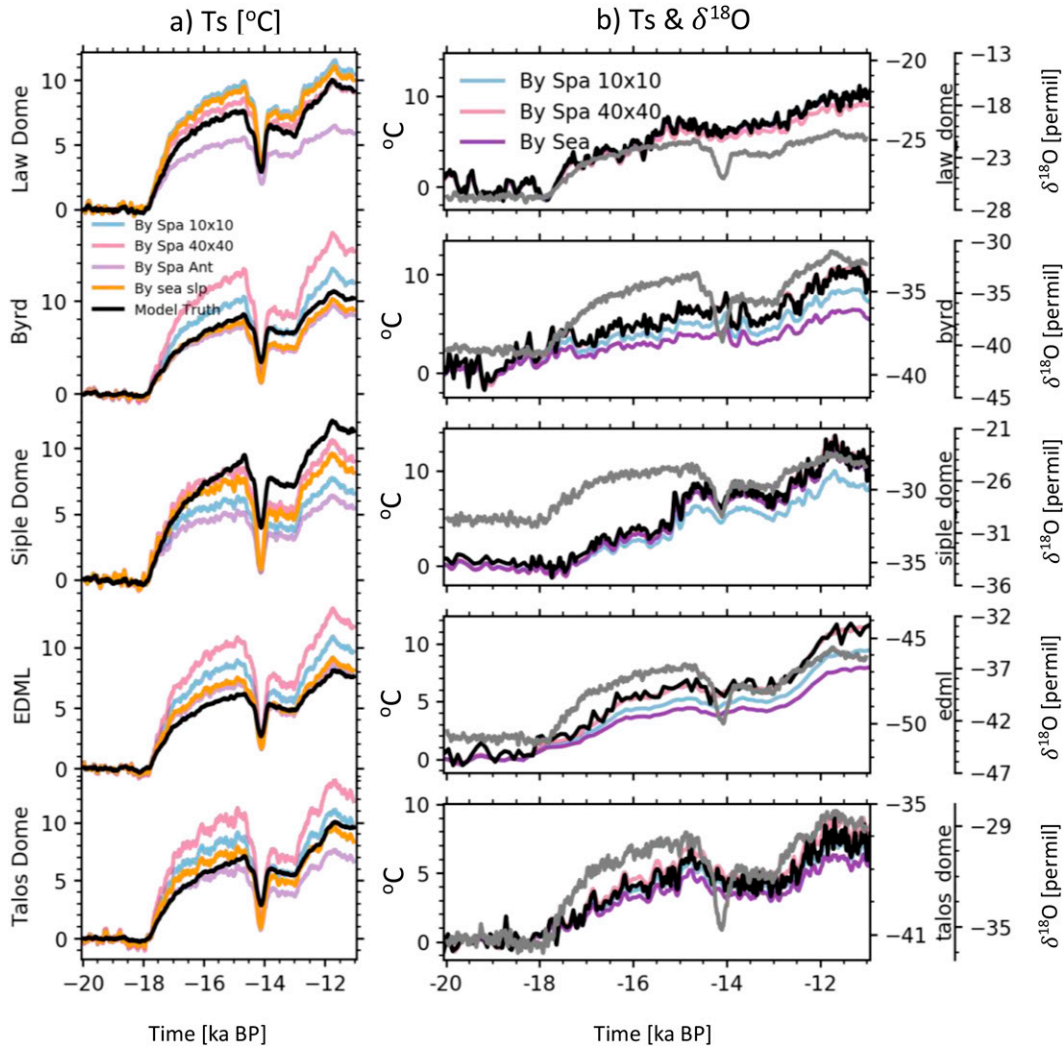


FIG. F1. Comparison of model  $T_s$  predicted using seasonal and spatial slopes from 20 to 11 ka. (a) Deglacial temperature evolution predicated with PI seasonal slope and three spatial slopes of different domain sizes (see legend) compared with the model truth (black) in five ice core sites. (b) Deglacial temperature evolution predicated using the model seasonal slope and three spatial slopes (see legend) on the observed  $\delta^{18}\text{O}$  (gray) along with model  $\delta^{18}\text{O}$  (black).

cores for the temperature change from 20 to 11 ka (Fig. F1b). As a test of the model simulation of isotope, we also note that the overall magnitude of the deglacial  $\delta^{18}\text{O}$  change from 20 to 11 ka is consistent in the model and observation over most sites, except that the model has too strong a response in HS1 across all sites. Since both the seasonal and spatial slopes here are based on iCESM and there is no true temperature time series for comparison, the comparison here is not to test the accuracy of the slopes. Rather, it is to reinforce the point of the modeling analysis that spatial slope is subject to large uncertainty of the domain choice.

#### REFERENCES

- Bailey, A., H. K. A. Singh, and J. Nusbaumer, 2019: Evaluating a moist isentropic framework for poleward moisture transport: Implications for water isotopes over Antarctica. *Geophys. Res. Lett.*, **46**, 7819–7827, <https://doi.org/10.1029/2019GL082965>.
- Boyle, E. A., 1997: Cool tropical temperatures shift the global  $\delta^{18}\text{O}$ -T relationship: An explanation for the ice core  $\delta^{18}\text{O}$ -borehole thermometry conflict? *Geophys. Res. Lett.*, **24**, 273–276, <https://doi.org/10.1029/97GL00081>.
- Braconnot, P., and Coauthors, 2011: The Paleoclimate Modeling Intercomparison Project contribution to CMIP5. *CLIVAR Exchanges*, No. 56, International CLIVAR Project Office, Southampton, United Kingdom, 15–19.
- , S. P. Harrison, M. Kageyama, P. J. Bartlein, V. Masson-Delmotte, A. Abe-Ouchi, B. Otto-Bliesner, and Y. Zhao, 2012: Evaluation of climate models using palaeoclimatic data. *Nat. Climate Change*, **2**, 417–424, <https://doi.org/10.1038/nclimate1456>.
- Brady, E., and Coauthors, 2019: The connected isotopic water cycle in the Community Earth System Model version 1. *J. Adv.*



- Model. Earth Syst.*, **11**, 2547–2566, <https://doi.org/10.1029/2019MS001663>.
- Buizert, C., and Coauthors, 2021: Antarctic surface temperature and elevation during the Last Glacial Maximum. *Science*, **372**, 1097–1101, <https://doi.org/10.1126/science.abd2897>.
- Cai, M., 2006: Dynamical greenhouse-plus feedback and polar warming amplification. Part I: A dry radiative-transportive climate model. *Climate Dyn.*, **26**, 661–675, <https://doi.org/10.1007/s00382-005-0104-6>.
- Charles, C. D., D. Rind, J. Jouzel, R. D. Koster, and R. G. Fairbanks, 1994: Glacial-interglacial changes in moisture sources for Greenland: Influences on the ice core record of climate. *Science*, **263**, 508–511, <https://doi.org/10.1126/science.263.5146.508>.
- Ciais, P., and J. Jouzel, 1994: Deuterium and oxygen 18 in precipitation: Isotopic model, including mixed cloud processes. *J. Geophys. Res.*, **99**, 16 793–16 803, <https://doi.org/10.1029/94JD00412>.
- Connolley, W. M., 1996: The Antarctic temperature inversion. *Int. J. Climatol.*, **16**, 1333–1342, [https://doi.org/10.1002/\(SICI\)1097-0088\(199612\)16:12<1333::AID-JOC96>3.0.CO;2-6](https://doi.org/10.1002/(SICI)1097-0088(199612)16:12<1333::AID-JOC96>3.0.CO;2-6).
- Cuffey, K. M., G. D. Clow, R. B. Alley, M. Stuiver, E. D. Waddington, and R. W. Saltus, 1995: Large Arctic temperature change at the Wisconsin-Holocene glacial transition. *Science*, **270**, 455–458, <https://doi.org/10.1126/science.270.5235.455>.
- , and Coauthors, 2016: Deglacial temperature history of West Antarctica. *Proc. Natl. Acad. Sci. USA*, **113**, 14 249–14 254, <https://doi.org/10.1073/pnas.1609132113>.
- Dansgaard, W., 1964: Stable isotopes in precipitation. *Tellus*, **16**, 436–468, <https://doi.org/10.1111/j.2153-3490.1964.tb00181.x>.
- Delworth, T. L., and Coauthors, 2020: SPEAR: The next generation GFDL modeling system for seasonal to multidecadal prediction and projection. *J. Adv. Model. Earth Syst.*, **12**, e2019MS001895, <https://doi.org/10.1029/2019MS001895>.
- Eriksson, E., 1965: Deuterium and oxygen-18 in precipitation and other natural waters: Some theoretical considerations. *Tellus*, **17**, 498–572, <https://doi.org/10.3402/tellusa.v17i4.9160>.
- Guan, J., Z. Liu, X. Wen, E. Brady, D. Noone, J. Zhu, and J. Han, 2016: Understanding the temporal slope of the temperature-water isotope relation during the deglaciation using iso-CAM3: The slope equation. *J. Geophys. Res. Atmos.*, **121**, 10 342–10 354, <https://doi.org/10.1002/2016JD024955>.
- He, C., and Coauthors, 2021a: Hydroclimate footprint of pan-Asian monsoon water isotope during the last deglaciation. *Sci. Adv.*, **7**, eabe2611, <https://doi.org/10.1126/sciadv.abe2611>.
- , Z. Liu, B. L. Otto-Bliesner, E. C. Brady, C. Zhu, R. Tomas, C. Buizert, and J. P. Severinghaus, 2021b: Abrupt Heinrich Stadial 1 cooling missing in Greenland oxygen isotopes. *Sci. Adv.*, **7**, eabh1007, <https://doi.org/10.1126/sciadv.abh1007>.
- Hendricks, M. B., D. J. DePaolo, and R. C. Cohen, 2000: Space and time variation of  $\delta^{18}\text{O}$  and  $\delta\text{D}$  in precipitation: Can paleotemperature be estimated from ice cores? *Global Biogeochem. Cycles*, **14**, 851–861, <https://doi.org/10.1029/1999GB001198>.
- Jouzel, J., and L. Merlivat, 1984: Deuterium and oxygen 18 in precipitation: Modeling of the isotopic effects during snow formation. *J. Geophys. Res.*, **89**, 11 749–11 757, <https://doi.org/10.1029/JD089iD07p11749>.
- , F. Vimeux, N. Caillon, G. Delaygue, G. Hoffmann, V. Masson-Delmotte, and F. Parrenin, 2003: Magnitude of isotope/temperature scaling for interpretation of central Antarctic ice cores. *J. Geophys. Res.*, **108**, 4361, <https://doi.org/10.1029/2002JD002677>.
- Kavanaugh, J. L., and K. M. Cuffey, 2003: Space and time variation of  $\delta^{18}\text{O}$  and  $\delta\text{D}$  in Antarctic precipitation revisited. *Global Biogeochem. Cycles*, **17**, 1017, <https://doi.org/10.1029/2002GB001910>.
- Kino, K., A. Okazaki, A. Cauquoin, and K. Yoshimura, 2021: Contribution of the Southern Annular Mode to variations in water isotopes of daily precipitation at Dome Fuji, East Antarctica. *J. Geophys. Res. Atmos.*, **126**, e2021JD035397, <https://doi.org/10.1029/2021JD035397>.
- Krinner, G., C. Genthon, and J. Jouzel, 1997: GCM analysis of local influences on ice core  $\delta$  signals. *Geophys. Res. Lett.*, **24**, 2825–2828, <https://doi.org/10.1029/97GL52891>.
- Lee, J.-E., I. Fung, D. J. DePaolo, and B. Otto-Bliesner, 2008: Water isotopes during the Last Glacial Maximum: New general circulation model calculations. *J. Geophys. Res.*, **113**, D19109, <https://doi.org/10.1029/2008JD009859>.
- Lorius, C., and L. Merlivat, 1975: Distribution of mean surface stable isotopes values in East Antarctica; observed changes with depth in coastal area. *General Assembly of the International Union of Geodesy and Geophysics*, Grenoble, France, International Union of Geodesy and Geophysics, 1–18, <https://www.iaea.org/resources/databases/inis>.
- Lu, F., and Coauthors, 2020: GFDL's SPEAR seasonal prediction system: Initialization and ocean tendency adjustment (OTA) for coupled model predictions. *J. Adv. Model. Earth Syst.*, **12**, e2020MS002149, <https://doi.org/10.1029/2020MS002149>.
- Lu, J., and M. Cai, 2010: Quantifying contributions to polar warming amplification in an idealized coupled general circulation model. *Climate Dyn.*, **34**, 669–687, <https://doi.org/10.1007/s00382-009-0673-x>.
- Markle, B. R., and E. J. Steig, 2022: Improving temperature reconstructions from ice-core water-isotope records. *Climate Past*, **18**, 1321–1368, <https://doi.org/10.5194/cp-18-1321-2022>.
- , and Coauthors, 2017: Global atmospheric teleconnections during Dansgaard–Oeschger events. *Nat. Geosci.*, **10**, 36–40, <https://doi.org/10.1038/ngeo2848>.
- Masson-Delmotte, V., and Coauthors, 2008: A review of Antarctic surface snow isotopic composition: Observations, atmospheric circulation, and isotopic modeling. *J. Climate*, **21**, 3359–3387, <https://doi.org/10.1175/2007JCL12139.1>.
- Motoyama, H., N. Hirasawa, and K. Satow, 2005: Seasonal variations in oxygen isotope ratios of daily collected precipitation and wind drift samples and in the final snow cover at Dome Fuji Station, Antarctica. *J. Geophys. Res.*, **110**, D11106, <https://doi.org/10.1029/2004JD004953>.
- Noone, D., 2008: The influence of midlatitude and tropical overturning circulation on the isotopic composition of atmospheric water vapor and Antarctic precipitation. *J. Geophys. Res.*, **113**, D04102, <https://doi.org/10.1029/2007JD008892>.
- , 2009: Kink in the thermometer. *Nature*, **462**, 295–296, <https://doi.org/10.1038/462295a>.
- Nusbaumer, J., T. E. Wong, C. Bardeen, and D. Noone, 2017: Evaluating hydrological processes in the Community Atmosphere Model version 5 (CAM5) using stable isotope ratios of water. *J. Adv. Model. Earth Syst.*, **9**, 949–977, <https://doi.org/10.1002/2016MS000839>.
- Schneider, D. P., E. J. Steig, and T. V. Ommen, 2005: High-resolution ice-core stable-isotopic records from Antarctica: Towards interannual climate reconstruction. *Ann. Glaciol.*, **41**, 63–70, <https://doi.org/10.3189/172756405781813357>.
- Severinghaus, J. P., T. Sowers, E. J. Brook, R. B. Alley, and M. L. Bender, 1998: Timing of abrupt climate change at the end of

- the Younger Dryas interval from thermally fractionated gases in polar ice. *Nature*, **391**, 141–146, <https://doi.org/10.1038/34346>.
- Siler, N., A. Bailey, G. H. Roe, and C. Buizert, 2021: The large-scale, long-term coupling of temperature, hydrology, and water isotopes. *J. Climate*, **34**, 6725–6742, <https://doi.org/10.1175/JCLI-D-20-0563.1>.
- Sime, L. C., J. C. Tindall, E. W. Wolff, W. M. Connolley, and P. J. Valdes, 2008: Antarctic isotopic thermometer during a CO<sub>2</sub> forced warming event. *J. Geophys. Res.*, **113**, D24119, <https://doi.org/10.1029/2008JD010395>.
- , E. W. Wolff, K. I. C. Oliver, and J. C. Tindall, 2009: Evidence for warmer interglacials in East Antarctic ice cores. *Nature*, **462**, 342–345, <https://doi.org/10.1038/nature08564>.
- Stenni, B., C. Sarchilli, and V. Masson-Delmotte, 2016: Three-year monitoring of stable isotopes of precipitation at Concordia Station, East Antarctica. *Cryosphere*, **10**, 2415–2428, <https://doi.org/10.5194/tc-10-2415-2016>.
- Thompson, L. G., and E. Mosley-Thompson, 2000: Ice-core palaeoclimate records in tropical South America since the Last Glacial Maximum. *J. Quat. Sci.*, **15**, 377–394, [https://doi.org/10.1002/1099-1417\(200005\)15:4<377::AID-JQS542>3.0.CO;2-L](https://doi.org/10.1002/1099-1417(200005)15:4<377::AID-JQS542>3.0.CO;2-L).
- Turner, J. P. T., and Coauthors, 2019: The dominant role of extreme precipitation events in Antarctic snowfall variability. *Geophys. Res. Lett.*, **46**, 3502–3511, <https://doi.org/10.1029/2018GL081517>.
- van Ommen, T. D., and V. Morgan, 1997: Calibrating the ice core paleothermometer using seasonality. *J. Geophys. Res.*, **102**, 9351–9357, <https://doi.org/10.1029/96JD04014>.
- Werner, M., U. Mikolajewicz, M. Heimann, and G. Hoffmann, 2000: Borehole versus isotope temperatures on Greenland: Seasonality does matter. *Geophys. Res. Lett.*, **27**, 723–726, <https://doi.org/10.1029/1999GL006075>.
- , J. Jouzel, V. Masson-Delmotte, and G. Lohmann, 2018: Reconciling glacial Antarctic water stable isotopes with ice sheet topography and the isotopic paleothermometer. *Nat. Commun.*, **9**, 3537, <https://doi.org/10.1038/s41467-018-05430-y>.